

The Effects of Dietary Ingestion of Nickel Recovery Slag as a Grit Source on Avian
Bone

By

Michel R. Lapointe

A thesis submitted in partial fulfilment
of the requirements for the degree of
Master of Science (MSc) in Physics

The Faculty of Graduate Studies
Laurentian University
Sudbury, Ontario, Canada

© Michel R. Lapointe, 2020

THESIS DEFENCE COMMITTEE/COMITÉ DE SOUTENANCE DE THÈSE
Laurentian Université/Université Laurentienne
Faculty of Graduate Studies/Faculté des études supérieures

Title of Thesis Titre de la thèse	The Effects of Dietary Ingestion of Nickel Recovery Slag as a Grit Source on Avian Bone	
Name of Candidate Nom du candidat	Lapointe, Michel	
Degree Diplôme	Master of Science	
Department/Program Département/Programme	Physics	Date of Defence Date de la soutenance June 5, 2020

APPROVED/APPROUVÉ

Thesis Examiners/Examineurs de thèse:

Dr. Eduardo Galliano
(Co-Supervisor/Co-directeur(trice) de thèse)

Dr. Robert Leclair
(Co-supervisor/Co-directeur(trice) de thèse)

Dr. Rob Lafrenie
(Committee member/Membre du comité)

Dr. Jeff Frimeth
(Committee member/Membre du comité)

Dr. Apichart Linhananta
(External Examiner/Examineur externe)

Approved for the Faculty of Graduate Studies
Approuvé pour la Faculté des études supérieures
Dr. David Lesbarrères
Monsieur David Lesbarrères
Dean, Faculty of Graduate Studies
Doyen, Faculté des études supérieures

ACCESSIBILITY CLAUSE AND PERMISSION TO USE

I, **Michel Lapointe**, hereby grant to Laurentian University and/or its agents the non-exclusive license to archive and make accessible my thesis, dissertation, or project report in whole or in part in all forms of media, now or for the duration of my copyright ownership. I retain all other ownership rights to the copyright of the thesis, dissertation or project report. I also reserve the right to use in future works (such as articles or books) all or part of this thesis, dissertation, or project report. I further agree that permission for copying of this thesis in any manner, in whole or in part, for scholarly purposes may be granted by the professor or professors who supervised my thesis work or, in their absence, by the Head of the Department in which my thesis work was done. It is understood that any copying or publication or use of this thesis or parts thereof for financial gain shall not be allowed without my written permission. It is also understood that this copy is being made available in this form by the authority of the copyright owner solely for the purpose of private study and research and may not be copied or reproduced except as permitted by the copyright laws without written authority from the copyright owner.

Abstract

Nickel recovery slag has been ubiquitously deposited in the environment of the Sudbury, Ontario basin giving merit to a study of the impact of this foreign material on wildlife in the area. In this work, the effects of ingestion of this largely metallic grit source on the bone health of *Columbia Livia Domestica* pigeons was measured. This was accomplished by controlling the diets of two groups of birds, one given exclusively limestone grit, the second given exclusively slag as a grit source. After one year of this controlled diet, the subjects were euthanized and their tibiotarsi were subsequently harvested for testing. Tests performed on the tibiotarsi including breaking strength, Young's modulus, cortical thickness, density, bone mineral density, and mass spectrometry with a focus on iron and calcium concentrations. Additionally, conventional micrographs and scanning electron micrographs with accompanying energy dispersive spectrometry were collected. Our analyses of the results are consistent with degraded bone physiology in the slag-fed group compared to the control birds.

Keywords: Mining, slag, avian, pigeon, bone, pollution, environment, diet, metabolism, iron, bone-mineral density, distance correlation, pearson distance, distance correlation distance.

Acknowledgments

I would like to thank my supervisor, Dr Eduardo Galiano-Riveros for providing me this opportunity for enriching research and his mentorship. A special thanks to my co-supervisor Dr Robert Leclair for his guidance, and discussion in the writing process and a number of academic ventures. Thank you to my supervisory committee for their guidance throughout the project. Thank you Alex Leblanc, Alex Robillard, Konnor Kennedy, and all graduate students in the Laurentian University Department of Physics who've assisted me in the construction and refinement of python scripts, as well as a number of discussions on topics of research and general interest. Last but certainly not least, a tremendous thank you to Amanda Daigle for constantly keeping me on track and giving me support and encouragement when it was needed.

Table of Contents

ABSTRACT	II
ACKNOWLEDGMENTS	III
LIST OF TABLES	VI
LIST OF ABBREVIATIONS	VII
LIST OF EQUATIONS	XIII
CHAPTER 1: INTRODUCTION	1
1.1 Background and Motivation	1
CHAPTER 2: TESTING PARAMETERS	4
2.1 Breaking Strength (Bone)	4
2.2 Young's Modulus (Bone).....	5
2.3 Cortical Bone Thickness (Bone)	6
2.4 Conventional Density (Bone)	7
2.5 Bone-Mineral Density (Bone).....	9
2.6 Calcium Concentration (Bone).....	16
2.7 Iron Concentration (Bone)	19
2.8 Optical Microscopy (Bone)	20
2.9 Scanning Electron Microscopy and Energy Dispersive Spectrometry (Bone)	21
2.10 Stone Hardness Testing (Grit).....	23
2.11 X-Ray Fluorescence (Slag)	26
2.12 Electrothermal Vaporization – Inductively Coupled Plasma – Optical Emission Spectrometry (Bone and Slag).....	29
CHAPTER 3: STATISTICAL METHODS	31
3.1 Welch's T-test	31
3.2 Pearson's Correlation	31
3.3 Distance Correlation	33
4.1 Quantitative Parameters	36
4.2 Qualitative (and semiquantitative) Parameters	45
4.3 Pearson Correlations	50
CHAPTER 5: CONCLUSIONS	60

REFERENCES.....	62
APPENDIX I	69
APPENDIX II	73

List of Tables

Table 1: Table of quantitative results, with number of sample measurements, and one-tail Welch's t-test values.	36
Table 2: Preliminary ETV-ICP-OES results, results are shown with standard deviation.....	44
Table 3: Mean EDS results, standard deviations are omitted given the small sample size (n=2) and as these results are provided for comparison with ETV-ICP-OES results.....	46
Table 4: Pearson correlation values for all control parameters.....	51
Table 5: Pearson correlation values for all experimental parameters.	51
Table 6: Pearson distance values for all parameters.....	51
Table 7: Distance correlations for control group.....	55
Table 8: Distance correlations for experimental group.	56
Table 9: Székely distances between control and experimental.....	57
Table 10: Table showing the results of differences from the proposed relationship of equation 24 for all bivariations found to be significant with the Pearson Correlation test. Notice that all values are near 0 (mean = -0.01).....	59

List of Abbreviations

BS	Breaking Strength
YM	Young's Modulus
TH	Thickness
CD	Conventional Density
BMD	Bone Mineral Density
DXA	Dual-Energy X-Ray Absorptiometry
Ca	Calcium Concentration
Fe	Iron Concentration
MS	Mass Spectrometry
n	Number of
p	T-Test Coefficient
R	Correlation Coefficient
R	Distance Correlation Coefficient
Var, dVar	Variance and distance Variance, respectively
Cov, dCov	Covariance and distance Covariance, respectively
OM	Optical Microscopy
SEM	Scanning Electron Microscopy
EDS	Energy Dispersive Spectrometry
CH	Calcium Hydroxyapatite
NTBI	Non-Transferrin Bound Iron
TOF	Time-of-Flight

List of Figures

Figure 1: Left, image of actual sample (seen in center) being compressed in the UTM. Right, image of bone sample after suffering a fault in the UTM.....	4
Figure 2: Basic Diagram of a Universal Testing Machine.....	5
Figure 3: Example of a Bone Sample on the UTM Table.....	5
Figure 4: Bone cross-section depicting the inner diameter (endosteum) and outer diameter (periosteum) measured for bone thickness.	7
Figure 5: ~2cm section of Diaphysis compact bone removed.	8
Figure 6: Left, prepared bone samples ready for weighing. Right, water filled flask weighed in the enclosed scale.....	9
Figure 7: Cerium-58 Mass Attenuation Coefficient as a function of primary photon energy on a log scale. Indicated in red is the relatively large increase in mass attenuation coefficient at 40keV, which is the K-shell binding energy of cerium- 58.....	11
Figure 8: Photon intensity in arbitrary units as a function of energy generated from a tungsten anode, aluminum filtered X-Ray tube with an 80kV accelerating potential. The red section is the energy range which will be peaked after transmission through a cerium-58 sheet.....	12
Figure 9: The spectrum from the same X-Ray tube in Figure 2 after passing through a 1.2mm Cerium-58 filter. The red section is the same energy range as is highlighted in the previous figure.....	12
Figure 10: Relative spectra without filtering, versus with 1.2mm of Cerium-58, and 1.2mm of Cerium-58, 0.06mm of bone, and 40mm of soft tissue.	13

Figure 11: A closer comparison of Cerium-58 filtered X-Ray tube spectra before and after passing through a volume of soft tissue and bone..... 13

Figure 12: Photo of a Lunar Prodigy DXA scanner similar to that used in this study. Indicated are the detector, patient table, and X-ray tube, located in the housing beneath the patient table. Image obtained from <https://medplusequipment.com/product/refurbished-ge-lunar-prodigy/>..... 15

Figure 13: Diagram of the basic mass spectrometer. Electric and magnetic field directions indicated by E and B respectively. 17

Figure 14: Perkin-Elmer Flame Atomic Absorption Spectrometer used in this study. Notice the open hatch revealing the atomizing portion..... 19

Figure 15: Left, vertical line representing the fault line of the mid-diaphysis cortical tibio-tarsi which was analyzed via SEM and EDS, and the ~1mm section of broken bone which was removed for OM. Right, image of the Nikon Optiphot reflection and transmission microscope used in this study. 21

Figure 16: Rough Schematic of a Scanning Electron Microscope equipped with EDS. 22

Figure 17: JEOL model 6400 Scanning Electron Microscope, similar to that used in this study..... 23

Figure 18: BHN diagram..... 24

Figure 19: RH Test diagram..... 25

Figure 20: Brinell Hardness testing apparatus (Louis Small Inc. Model 8BLP Brinell Hardness Tester, Cincinnati, OH, USA) used in this study..... 25

Figure 21: Diagram of iron atom. Electron K-shell depicted in red, L-shell in blue, and M-shell in green. K-alpha and K-beta transitions are indicated..... 27

Figure 22: X-Ray fluorescence diagram showing detector, sample, and X-Ray tube. 28

Figure 23: Image of the X-Ray Fluorescence set-up used in this experiment. The slag sample can be observed at the center of the image (black object on metal cylinder). At the left of the image is located the Intrinsic Cryogenic Germanium Detector..... 29

Figure 24: Depiction of distance matrix, where x is some parameter, and the subscripts 1 through n indicate the sample number..... 35

Figure 25: Results from Thickness measurements plotted from lowest to highest for comparison with experimental results in red and control in green. 37

Figure 26: Results from Conventional Density measurements plotted from lowest to highest for comparison with experimental results in red and control in green.38

Figure 27: Results from Bone Mineral Density measurements plotted from lowest to highest for comparison with experimental results in red and control in green.39

Figure 28: Results from Calcium Concentration measurements plotted from lowest to highest for comparison with experimental results in red and control in green. 40

Figure 29: Results from Iron Concentration measurements plotted from lowest to highest for comparison with experimental results in red and control in green.41

Figure 30: Results from Breaking Strength measurements plotted from lowest to highest for comparison with experimental results in red and control in green.42

Figure 31: Results from Young’s Modulus measurements plotted from lowest to highest for comparison with experimental results in red and control in green.43

Figure 32: Histogram depicting the full quantitative data set in relative units with relative error bars. The control group set to unity for all but Fe. 43

Figure 33: All ETV-ICP-OES results shown in relative units to compare control samples with experimental..... 45

Figure 34: a) Electron micrograph of representative control sample. B) Electron micrograph of representative experimental sample with visible cavitations and loss of the granular architecture that is clearly visible in a). 45

Figure 35: a) Optical micrograph of representative experimental sample along a fault after UTM testing. Note the brown coloring, which may be the result of higher iron content, and the frayed edges along the periosteum and endosteum. B) Optical micrograph of representative control bone along fault line after UTM testing. Note here the milky white color and sharp edges along the periosteum and endosteum..... 47

Figure 36: Optical micrographs of experimental samples. On the left, notice parallel-arranged spicules and cavities. On the right, a red-brown localized circular deposit, approximately 40µm in diameter, many of which were found in experimental samples, none in control..... 48

Figure 37: Energy spectrum from X-Ray Fluorescence of slag acquired with intrinsic Germanium cryogenic detector. a) Peak of the 6.4keV K-alpha characteristic emission from iron fluorescence. b) Peak of the 6.9keV K-beta characteristic

emission from iron fluorescence. c) Energy spectrum resulting from Compton Scattering within the detector..... 50

Figure 38: Despite the low number of measurements for this bivariate comparison (n=3), a linear relationship is observed. 55

Figure 39: Scatter plot of Calcium Concentration data and Iron Concentration data from the experimental group. The 'shape' of the data can be observed. 56

Figure 40: Scatter plot showing the control BMD-Ca results in green, and experimental results for the same parameters in blue. There is a more evident shape in the green (control) data, as most of the blue (experimental) data lie very nearly constant along the x-axis (BMD) while spreading wide along the y-axis (Ca)..... 57

Figure 41: Plot of energy transmission spectra after passing through the highest TH (0.73mm), and lowest TH (0.43mm). 58

List of Equations

Equation 1: YM-BS relationship, where r is the measurement of radius, l is the length of the sample, and d is the compression distance.....	6
Equation 2: Volume equation based on the Archimedes principle, where V_B is the volume of the bone, D_w is the density of water at 22°C.....	8
Equation 3: Conventional density.....	9
Equation 4: Two photon beam transport equations. The superscript 'h' indicates high beam energy and 'l' indicates low beam energy. Subscript 's' indicates soft tissue and 'b' indicates bone. M is the BMD of the subscripted material.....	14
Equation 5: BMD equation for a theoretical two-compartment model.....	14
Equation 6: Centripetal Force. M = mass, v = velocity, r = path radius.....	18
Equation 7: Magnetic Force. Q = charge of particle, B = magnetic flux density.	18
Equation 8: By setting both forces to equilibrium, we solve for r	18
Equation 9: Reduced relationship between radius and mass, with intervening velocity.....	18
Equation 10: Brinell Hardness Number (BHN) equation, where P = applied load (kgf), D = indenter diameter (mm), and d = diameter of indentation (mm).	24
Equation 11: Rockwell Hardness value (RH), where N = scaling factor, $d = d_0 - d_1$ (penetration depth), and s = scaling factor.....	25
Equation 12: Variance equation, where N is the number of samples measured for the parameter in question, x is the measured value of sample I , and μ is the mean value of this sample set for the parameter in question.	32

Equation 13: Covariance equation, where y is the second parameter value of sample I , and v is the mean value of y for the samples in question.....	32
Equation 14: Correlation.	32
Equation 15: Distance between sample j and sample k of parameter x	34
Equation 16: 'j' data centering equation. Equivalent to the mean distance for sample 'j'.....	34
Equation 17: Parametric centering equation. Equivalent to mean distance for all data points of parameter 'x'.....	34
Equation 18: Full centering/normalization.....	34
Equation 19: Distance variance.	34
Equation 20: Distance covariance.....	34
Equation 21: Distance correlation.....	34
Equation 22: Distance Correlation distance.....	35
Equation 23: Limits of the Distance Correlation distance.....	35
Equation 24: Relationship between R and R if the correlation between parameters is linear.....	59

Chapter 1: Introduction

1.1 Background and Motivation

The Sudbury basin has been a focus of nickel mining activity for more than 100 years, resulting in significant changes to the natural environment. A most notable change is the presence/dumping of nickel recovery slag in the otherwise pristine environment [1, 2, 29]. This slag, which presents as dense, metallic gravel/stone, can be found in varying size and shape in areas surrounding the city of Sudbury [1, 2]. This substance has the potential to cause harm to local wildlife [1,29]. One such pathway of harm arises from the relatively high iron concentration of the material in comparison to pristine stone (slag iron concentration $\sim 350000\mu\text{g/g}$, gravel iron concentration $\sim 750\mu\text{g/g}$) [1]. It follows then, that any grit dependent granivorous species in the area, such as the pigeon or ruffed grouse, will be liable to suffer from an iron overload if this substance is consumed [1, 29]. Iron overload is a condition which may result from a high iron concentration diet, resulting in a slew of symptoms in humans and animals, including but not limited to: liver disease, heart failure, and decreased overall bone health and osteoporosis [1, 19, 29, 47].

In an attempt to quantify the extent of harm a slag dependent diet can cause, we build on the research of Parker et al. by comparing the results of a number of tests on the bones of pigeons which have been given a highly controlled slag-based diet, with a group given a pristine limestone-based diet, as grit material [1, 29]. This was accomplished by taking a number of pigeons, four to ten weeks of age, and

separating them into two groups, one given exclusively a pristine gravel grit, the other, given exclusively slag based grit for ingestion with a grain based diet [1, 29]. This feeding period lasted one year, after which the subjects were euthanized, and their tibiotarsi harvested for testing [1, 29].

Chapter 2 will review the following testing parameters along with the measurement procedures that were done and how they can be useful in characterization of bone status. They are: measurement of breaking strength (BS), Young's modulus (YM), cortical bone thickness (TH), conventional mass density (CD), bone mineral density (BMD), calcium and iron concentration (Ca) and (Fe) respectively [29]. Additional qualitative testing of the bones involved optical microscopy (OM) and scanning electron microscopy (SEM) with energy dispersive spectrometry (EDS) [29].

In addition, hardness testing of the two grit types was measured using two hardness-testing methods; the Brinell Hardness Test (BHN) and the Rockwell hardness test (RH). X-Ray fluorescence measurements were taken for a representative sample of slag. Electrothermal Vaporization - Inductively Coupled Plasma - Optical Emission Spectrometry (ETV-ICP-OES) was performed in collaboration with Diane Beauchemin and Margaret MacConnachie at Queen's University, analyzing sulfur, calcium, and iron content of both bones, and slag samples. Although the effect of sulfur content in bones is not known, it was deemed of interest given a difference in sulfur concentration results from EDS. All the collected data was assembled to perform a qualitative, quantitative, and statistical analysis.

The statistical parameters used in this project include the Welch's t-test for testing of the significance of the change in all quantitative parameters between the control and experimental means. The Pearson Correlation test was used to test for linear correlation between pairs of parameters, and a Pearson Correlation distance was used to quantify changes in correlation between the control and experimental groups. The novel Distance Correlation parameter was used to test for non-linear correlation between all parametric bivariate correlations, and in analogy to the Pearson correlation distance, we introduce the Distance Correlation distance as a measure of changes in Distance Correlation [29]. This Distance Correlation distance was again found for all bivariate pairings for comparison of both groups.

Chapter 2: Testing Parameters

2.1 Breaking Strength (Bone)

Breaking strength BS is defined as the maximal axial force in compression or tension, to which a specimen can be subjected without failure, and is measured in units of Newtons (N) [5]. This is an essential measurement of bone health since it is a direct measure of the bone's primary function as a load-bearing structure [13, 14]. For both BS and YM, a Universal Testing Machine (UTM) (Tinius Olsen Model 2000 SL UTM, Horsham, PA, USA) was used (figures 12-14). This system is commonly used for the measurement of BS and YM in Material and Engineering sciences. It consists of a 500 kN hydraulic press and a solid table/base onto which the sample is placed and compressed. The provided software registers data on the applied force and compression of the material, plotting a stress-strain curve up to the point of failure/fracture of the material. The force applied at the point of failure is registered as the BS.



Figure 1: Left, image of actual sample (seen in center) being compressed in the UTM. Right, image of bone sample after suffering a fault in the UTM.

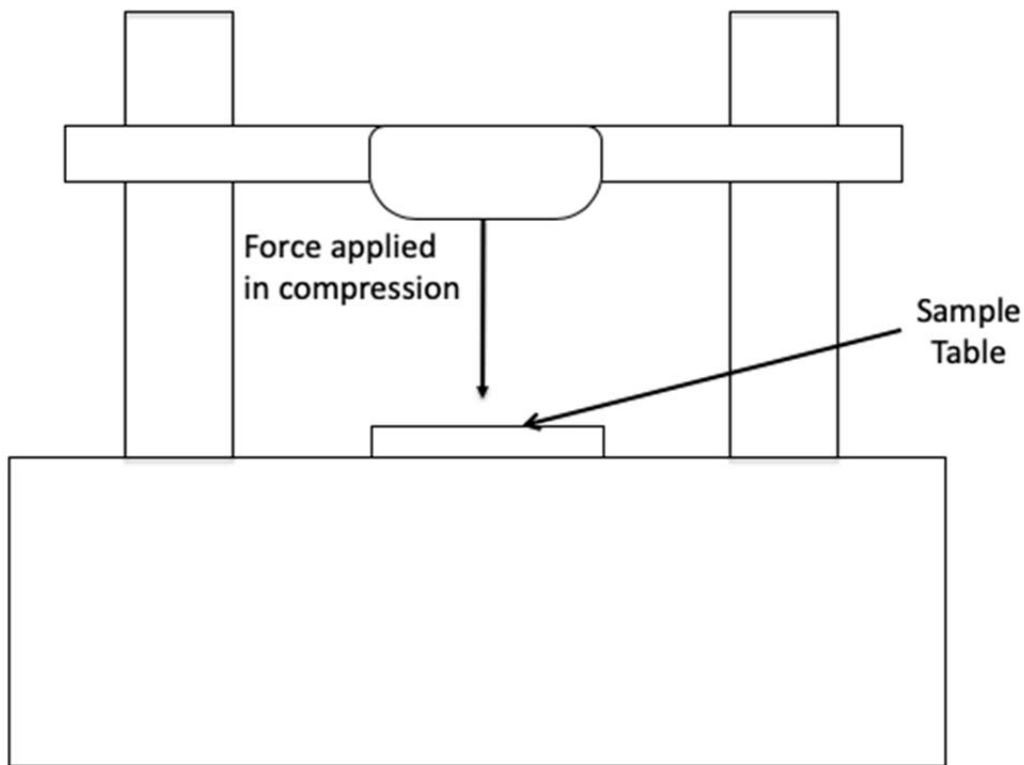


Figure 2: Basic Diagram of a Universal Testing Machine.

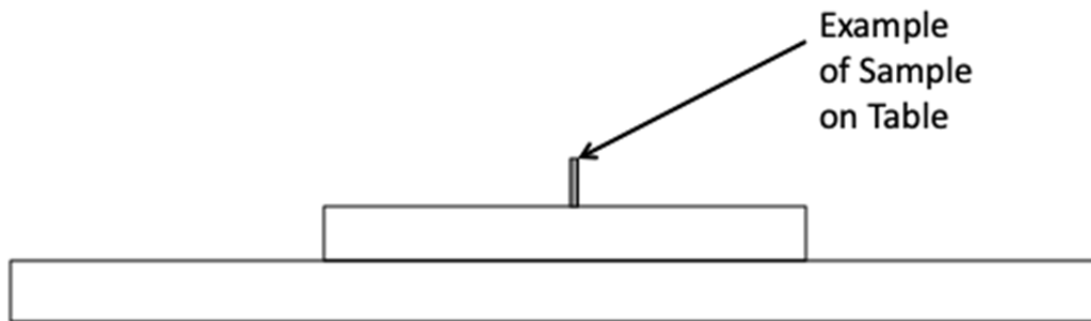


Figure 3: Example of a Bone Sample on the UTM Table.

2.2 Young's Modulus (Bone)

Young's Modulus Y_M is a physical quantity defining the elasticity of a solid material [5]. It is an analog of Hooke's constant for springs and is formally defined as the ratio of a solid's stress to its strain. It can be measured under compression or tensile forces in units of Pascal (Pa), or in our case Megapascal (MPa). It is an important measure for our purposes, as any change in this value associated with the dietary

intake of slag grit might indicate a physiological change in the formation or maintenance of the bony matrix [29].

From the registered UTM data, a best-fit value is given for YM, (in Mpa). Equation 9 shows the relationship between BS and YM, which is the basis of correlation between the two values discussed later.

Equation 1: YM-BS relationship, where r is the measurement of radius, l is the length of the sample, and d is the compression distance.

$$YM = \frac{BS * l}{\frac{\pi}{4}(r_{outer}^2 - r_{inner}^2) * d}$$

2.3 Cortical Bone Thickness (Bone)

Cortical bone thickness, TH, is a direct measurement of the thickness of the cortical – or load bearing - component of a long bone. It is a more direct measure of potential physiological changes in the bone, i.e. bone loss, or bone-growth impairment associated with dietary modifications. It was measured using a caliper, in units of millimeters (mm) [29].

Three measurements with a caliper (Mitsuyo model 500-196-30, Mitsuyo America Corporation, Aurora IL) were taken along the tibio-tarsus, for the inner radius and the outer radius as shown in figure 15. The mean of these three measurements was used as the value for TH, by subtracting the inner radius from the outer radius. This value is used in the statistical analysis of bone thickness, and the radius values are used in equation 9 to calculate the area for YM.

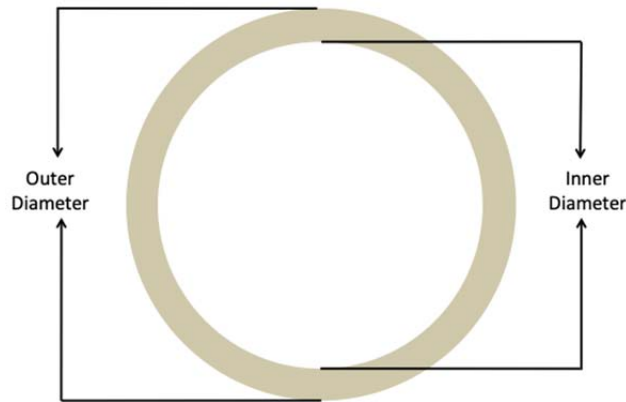


Figure 4: Bone cross-section depicting the inner diameter (endosteum) and outer diameter (periosteum) measured for bone thickness.

2.4 Conventional Density (Bone)

Conventional density, CD, is the ratio of the mass of an object to its volume, related to both the structural nature and elemental composition of the material. Changes here would be indicative, once again, of bone loss or compromised bone formation [14, 41]. This parameter was closely compared to the results of microscopy, which found a correlation between lower CD and the generally porous appearance in cross-sections of bone in the experimental group. It was measured and reported here in grams per cubic centimeter (g/cm^3) [29].

CD was measured using a specific gravity flask, and an enclosed scale (Escali Model L-125, Escali Corp., Burnville, MN, USA) to measure the volume and mass of the samples. A Dremel tool (Dremel Model 4300-9/64 High Performance Variable Speed Rotary Tool, Dremel Inc. Racine, WI, USA) was first used to cut out a 2-2.5cm long section of the diaphysis (Figure 16). All marrow was then removed from the inside of the hollow cylinder of bone. At this point, the bone was dried for 48 hours at 65°C . Once dried the bone was weighed in an enclosed scale (to prevent air movement

over the relatively small sample), and thus the dried bone mass was determined (M_B).

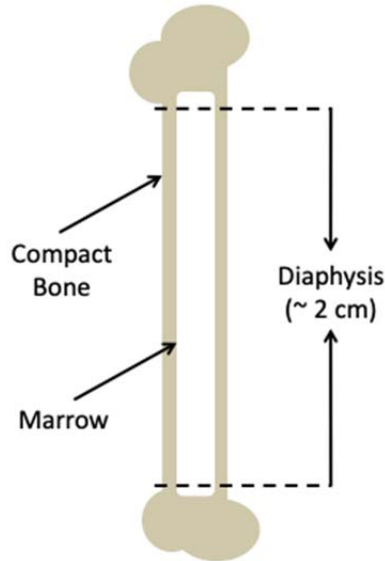


Figure 5: ~2cm section of Diaphysis compact bone removed.

Next, to determine the volume of the sample, a 25mL Pyrex specific gravity flask was filled with room temperature water ($\sim 21^\circ\text{C}$), and its mass was then measured (M_{FW}). Next, the dried bone was lightly inserted into the filled flask and allowed to saturate (eliminating all air bubbles adhering to the bone and allowing water to displace all air in the porous spaces of the bone) under vacuum. The water and bone filled flask weight was then measured (M_{FWB}). As the mass of the dry bone was known, we could use the following equations to determine CD:

Equation 2: Volume equation based on the Archimedes principle, where V_B is the volume of the bone, D_w is the density of water at 22°C .

$$V_B = \frac{M_{FW} - M_{FWB} + M_B}{D_w}$$

Equation 3: Conventional density.

$$CD = \frac{M_B}{V_B}$$



Figure 6: Left, prepared bone samples ready for weighing. Right, water filled flask weighed in the enclosed scale.

2.5 Bone-Mineral Density (Bone)

Bone mineral density, BMD, is a radiological measurement of the relatively high atomic number material (or bone mineral) to low atomic number material (or soft tissue) in a sample or patient [4]. It provides us with information as to the 2-dimensional calcium concentration of bone, which is heavily associated with general bone health and breaking strength, and is reported in units of grams per square centimeter (g/cm^2) [14, 17]. It is the accepted standard for the clinical diagnosis of osteoporosis in humans [38]. A small simulation was used to better describe this procedure.

A Lunar Prodigy DXA device was used for these measurements. This device uses a Cerium-58 filtered X-Ray tube to generate a 'virtual dual-energy beam' of X-Rays,

figure 1 shows the mass attenuation coefficient of cerium with respect to photon energy [48]. Calculated energy spectra without, and with such filtering are shown in figures 2 and 3 respectively. This 'virtual dual-energy beam' is possible as a result of the K-edge electron binding energy of Cerium-58, plotted in figure 1 and highlighted in red [6]. This generates maximum attenuation for photons of energies equal to, and just above the value of this binding energy of roughly 40keV. The beam is directed at a sample (or patient) and the transmitted energy distribution, an example of which is shown in figure 5, is analyzed to infer a ratio of the low to high atomic number material in the observed area. Given the Cerium-58 K-edge electron binding energy of $\sim 40\text{keV}$, there is a relatively large cross-section for the photoelectric effect of photons with energy equal to, or just above 40keV. What we're left with after transmission/filtering through a thin sheet of Cerium-58 is an X-Ray beam with two distinct energy peaks, a sharp one at just under 40keV, and another rounder peak between 70-80keV, as shown in figure 3. Given the photoelectric effect mass attenuation coefficient (τ/ρ) in the energy range around and below 100kV relates to the cubed ratio of the atomic number of the absorbing material (Z) and the energy of the interacting photon (E): $\tau/\rho \propto (Z/E)^3$, we can infer a ratio of low to high atomic number based on the observed ratio of low-energy photon ($\sim 40\text{keV}$) attenuation to high-energy photon (70-80keV) attenuation [6, 57]. This is visualized in figure 5 in which is plotted the beam energy spectrum as a function of incident photon energy just after filtering, and after transmission through a sample of similar dimensions to those used in our work. A relative decrease in both peaks is observed. Figure 4 shows the energy spectra of a tungsten

anode X-Ray beam without filtration, with 1.2mm of cerium filtering, and 1.2mm of cerium with 0.06mm of bone, and 40mm of soft tissue. Figure 5 shows a better view of the cerium filtered, and sample transmitted spectra. All values of mass attenuation coefficients were obtained from the NIST database using a script from the xpecgen package, shown in appendix I and II [45, 46]. All X-Ray energy spectra were generated using the xpecgen package in python [45]. Graphing was accomplished using the matplotlib package [46].

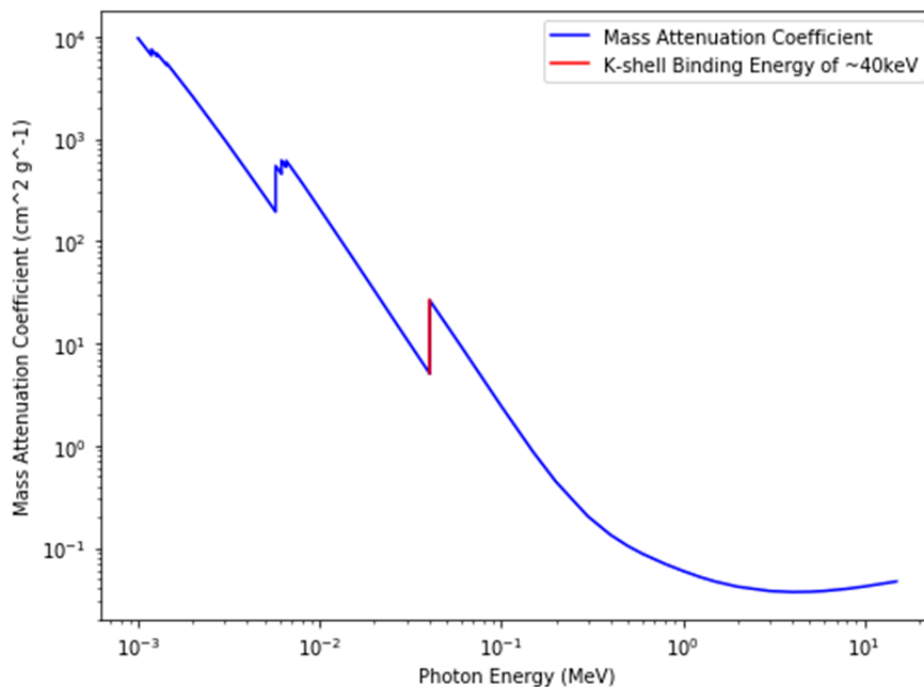


Figure 7: Cerium-58 Mass Attenuation Coefficient as a function of primary photon energy on a log scale. Indicated in red is the relatively large increase in mass attenuation coefficient at 40keV, which is the K-shell binding energy of cerium-58.

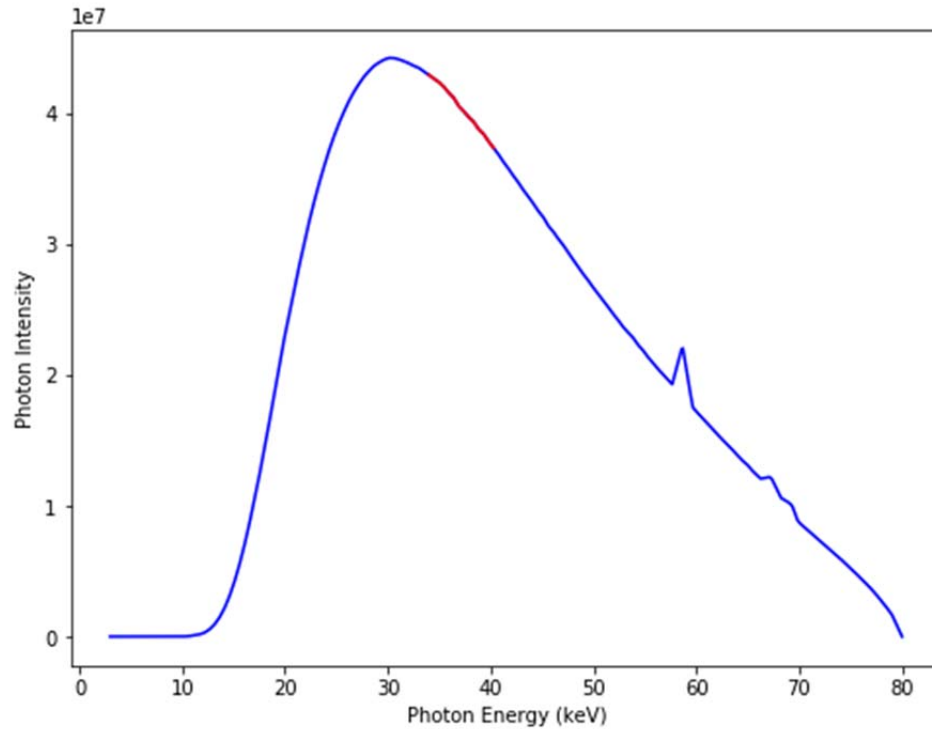


Figure 8: Photon intensity in arbitrary units as a function of energy generated from a tungsten anode, aluminum filtered X-Ray tube with an 80kV accelerating potential. The red section is the energy range which will be peaked after transmission through a cerium-58 sheet.

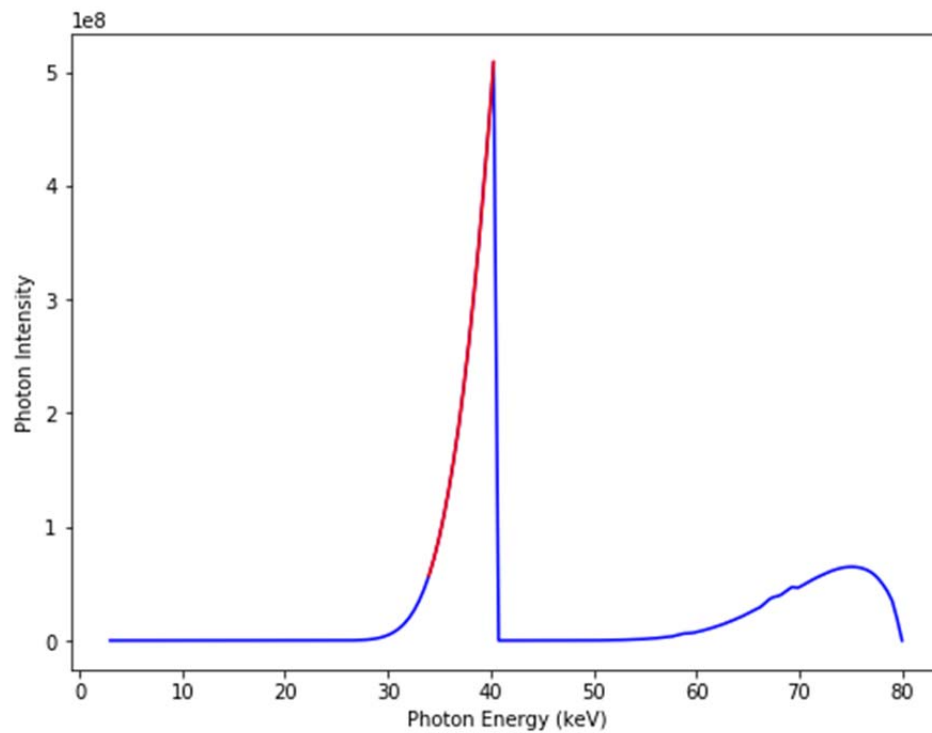


Figure 9: The spectrum from the same X-Ray tube in Figure 2 after passing through a 1.2mm Cerium-58 filter. The red section is the same energy range as is highlighted in the previous figure.

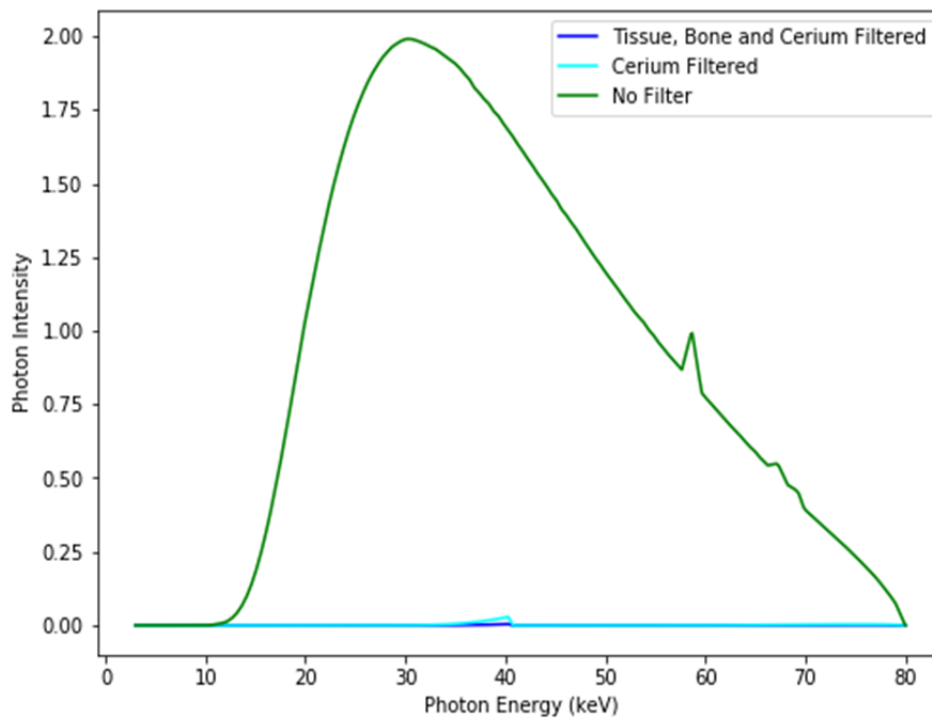


Figure 10: Relative spectra without filtering, versus with 1.2mm of Cerium-58, and 1.2mm of Cerium-58, 0.06mm of bone, and 40mm of soft tissue.

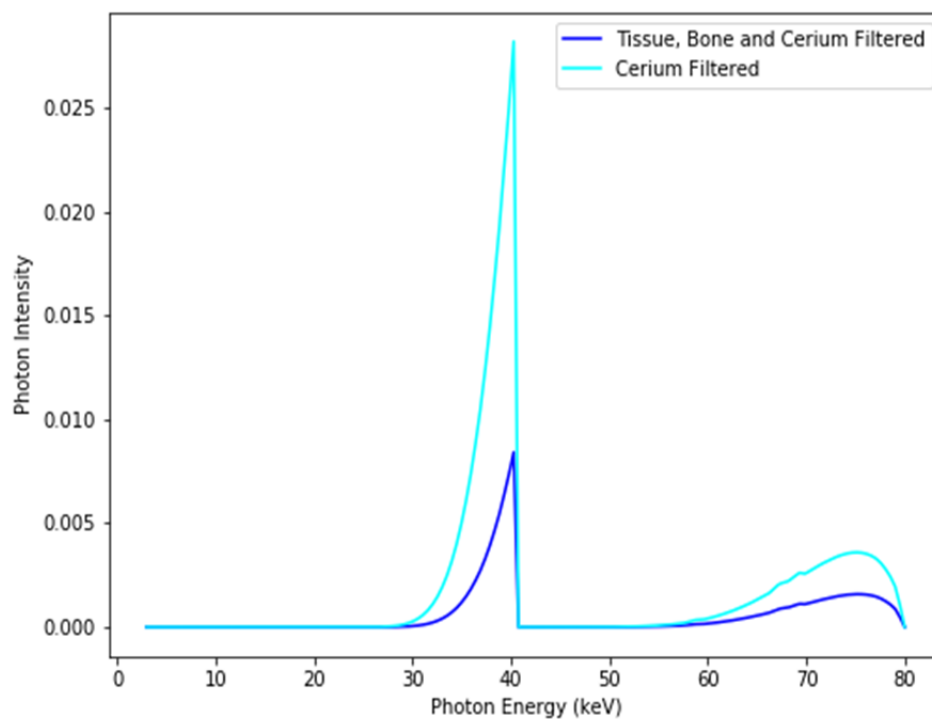


Figure 11: A closer comparison of Cerium-58 filtered X-Ray tube spectra before and after passing through a volume of soft tissue and bone.

For a theoretical understanding of this quantitative imaging modality, we can consider two independent photon beam transport equations from Frimeth, et. al. [42]:

Equation 4: Two photon beam transport equations. The superscript 'h' indicates high beam energy and 'l' indicates low beam energy. Subscript 's' indicates soft tissue and 'b' indicates bone. M is the BMD of the subscripted material.

$$N^h = N_o^h * e^{-[(\frac{\mu}{\rho})_s^h * M_s + (\frac{\mu}{\rho})_b^h * M_b]}$$

$$N^l = N_o^l * e^{-[(\frac{\mu}{\rho})_s^l * M_s + (\frac{\mu}{\rho})_b^l * M_b]}$$

Equation 2 shows that M_b will be in the proper BMD units of g/cm^2 . These will provide information on the attenuation of the two beams through a combination of soft tissue and bone. It is noted that M_s and M_b values are the same in both equations; therefore by solving for M_b we find the following relationship [42]:

Equation 5: BMD equation for a theoretical two-compartment model.

$$M_b = \frac{\ln \left[\left(\frac{N^h}{N_o^h} \right) * \left(\frac{\mu}{\rho} \right)_s^l \right] - \ln \left[\left(\frac{N^l}{N_o^l} \right) * \left(\frac{\mu}{\rho} \right)_s^h \right]}{\left(\frac{\mu}{\rho} \right)_b^l * \left(\frac{\mu}{\rho} \right)_s^h - \left(\frac{\mu}{\rho} \right)_b^h * \left(\frac{\mu}{\rho} \right)_s^l}$$

If we assume that both energies are constant for all scans (as they would be in a perfect system), then the BMD value will change only as the beam transport ratios change (unless they change in a proportionately inverse fashion). Further, if we assume negligible differences in sample thickness, knowing that the 'N/N_o' ratios

depend on the mass attenuation coefficients of the bone and soft tissue, we can see that this is a purely material dependent system [42].

BMD was measured using the aforementioned Dual-energy X-ray absorption (DXA) scanner (Lunar Prodigy Advance model PA 301850, GE Healthcare, Madison, WI). This is a clinical unit designed for use on humans and relies heavily on software that makes certain assumptions about the anatomy. Therefore, it was necessary to find and use a system preset that could provide accurate and consistent results in the pigeon bones, which are of considerably smaller volume than those for which the system is designed. A setting of: “52.9 yrs of age, female, 150lbs, AP Spine” was found to deliver consistent results. Additionally, since this technique relies on an assumed two-compartment model of anatomy (bone mineral and soft tissue), it requires a soft tissue substitute in order to function with the excised, marrow-removed pigeon bones used in our experiment. To simulate soft tissue, we covered the bones with bags of white rice; this satisfied the software requirements and allowed for consistent results.



Figure 12: Photo of a Lunar Prodigy DXA scanner similar to that used in this study. Indicated are the detector, patient table, and X-ray tube, located in the housing beneath the patient table. Image obtained from <https://medplusequipment.com/product/refurbished-ge-lunar-prodigy/>.

2.6 Calcium Concentration (Bone)

Calcium is the main structural component of the bony matrix (in its bio-molecular form of calcium hydroxyapatite) [9]. Impaired calcium metabolism would undoubtedly result in hampered bone formation, strength, and maintenance [3, 9, 10]. Therefore by measuring the calcium concentration (Ca) we can infer the possibility of problems in metabolism, and perhaps predict anatomical, structural, and mechanical changes (BS, YM, TH, and CD). Ca was measured on the right side tibiotarsus only, using mass spectrometry (MS), obtaining data in units of parts per million (PPM). MS is a highly precise and specific method for elemental analysis of materials, relying on mass to charge ratios of ionized samples of the material. However, it is an inherently destructive process, therefore multiple measurements of a small sample is not always possible. As shown in figure 6, a mass spectrometer generally functions in five steps:

- First, the prepared sample is vaporized.
- Second, the vaporized sample is singly ionized.
- Third the ionized sample is accelerated in a combination of electric fields and magnetic fields.
- Fourth, the path of the filtered particulate is curved precisely with an applied magnetic field. As the radius of curvature of the path in a magnetic field is dependent on the ratio of mass to charge, the sample is decomposed into its elemental constituents.

-The fifth step consists of simply detecting the ionized, accelerated, and filtered sample. This is accomplished with an array of negatively charged plates placed in the path forced upon the ions by the applied magnetic field. Every time a positively charged sample ion comes into contact with the negatively charged detector plate, an exchange of electrons occurs, which generates a potential difference in the circuitry. This is registered as a 'hit', and these are counted. The ratio of hits at a certain position on the detector plate to all other detections provides the concentration of material with the mass/charge ratio in question.

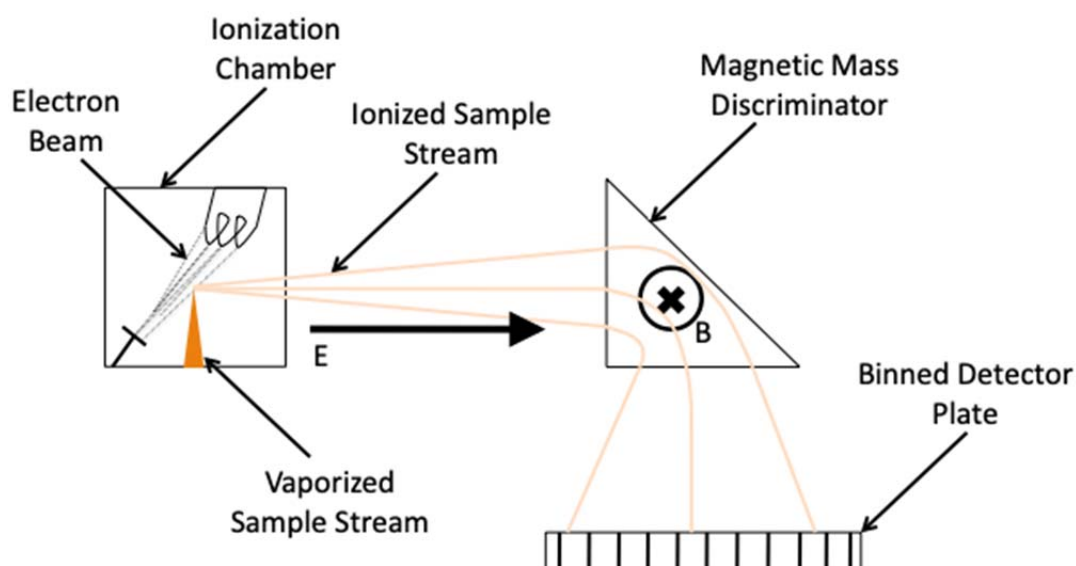


Figure 13: Diagram of the basic mass spectrometer. Electric and magnetic field directions indicated by E and B respectively.

For a closer look at the magnetic separation of elements, we can use the following two equations for centripetal and magnetic forces respectively:

Equation 6: Centripetal Force. $M = \text{mass}$, $v = \text{velocity}$, $r = \text{path radius}$.

$$F_c = \frac{mv^2}{r}$$

Equation 7: Magnetic Force. $Q = \text{charge of particle}$, $B = \text{magnetic flux density}$.

$$F_m = q\vec{v} \times \vec{B}$$

Since the magnetic force is equal to the centripetal force in this system, we can set them in equilibrium to find the value of the radius.

Equation 8: By setting both forces to equilibrium, we solve for r .

$$r = \frac{mv}{qB}$$

Since we assume all elements are singly ionized (which is generally true) the value of charge is constant along with the magnetic flux density of the system. Therefore we can reduce the equation into a relationship in which we keep only the values that vary from one element to another.

Equation 9: Reduced relationship between radius and mass, with intervening velocity.

$$r \propto mv$$

Mass is evidently the crucial variable for which we want sensitivity. Therefore the velocity must be in some manner accounted for. This is usually accomplished via time of flight filtration (TOF). Since the ion is accelerated first in an electric field, there is some variability in the acceleration felt depending on the elemental mass. Therefore, TOF can ensure that only ions of a narrow range of velocities are permitted to enter the magnetic field filtering stage.

(Ca) and (Fe) were measured with MS (Perkin-Elmer Model 7.03 flame atomic absorption spectrometer, Shelton, CT, USA). Samples were prepared as follows: all

right side tibiotarsi ($n = 9$ for both groups, $n = 18$ total) were fragmented into small pieces, and all fat inclusions removed. Samples weighing $0.5 \pm 0.01\text{g}$ were digested in 6.4mL of HNO_3 and 1.6mL of H_2O_2 (30%) using pulsatile microwave heating (EMS-820 Precision Pulsed Laboratory Microwave Oven, Hatfield, PA, USA), and then brought to a volume of $25.0 \pm 0.1\text{mL}$ with deionized water. At this point, the sample was used for analysis in the mass spectrometer.

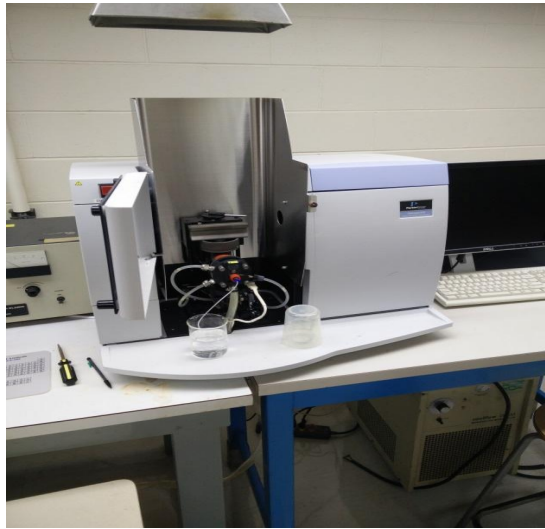


Figure 14: Perkin-Elmer Flame Atomic Absorption Spectrometer used in this study. Notice the open hatch revealing the atomizing portion.

2.7 Iron Concentration (Bone)

Iron concentration (Fe) was also measured through MS in units of PPM, with the same samples used for **1.2.6**. Given that the grit that was consumed by the experimental group of pigeons had a relatively high concentration of iron, it was deemed important to quantify iron uptake in bone. If a considerably higher level of Fe was found in the experimental group, then we could infer that some level of hemosiderosis (also known as iron storage disease) could be caused by the modified (slag) diet [1, 15].

Methods for this measurement can be found in section (2.6).

2.8 Optical Microscopy (Bone)

Optical microscopy (OM) is an integral aspect of any assessment of pathology. A precise visual assessment of the samples in question can often provide some much-needed context to the raw data obtained through quantitative measurement. In this case, we've been able to corroborate the results of measurements of TH, and CD with our optical micrographs. The former is evident as bone thickness can be observed visually; the latter can be ascertained as higher observed porosity in the experimental bone was correlated with a decreased value of CD.

For OM, a microscope (Nikon Upright Optiphot Model 200 microscope, Nikon Inc. Shinagawa, Tokyo, Japan, equipped with a Proscope model HR camera, Proscope Inc., Oregon City, OR, USA) was used to analyze the broken fragments of bone, as well as cross-sectional dissections of the hollow cylinder of the diaphysis. To view these cross-sections, a Stanley 5IN hobby knife was used to dissect a roughly one-millimeter long section of the proximal or distal portion of the diaphysis (refer to Figure 20), which was then placed under the reflecting microscope for analysis. Additional microscopy was performed on the lengthwise faults (Figure 20) of the bone after use of UTM. This was accomplished using the same Nikon Optiphot microscope as for the cross-section analysis.

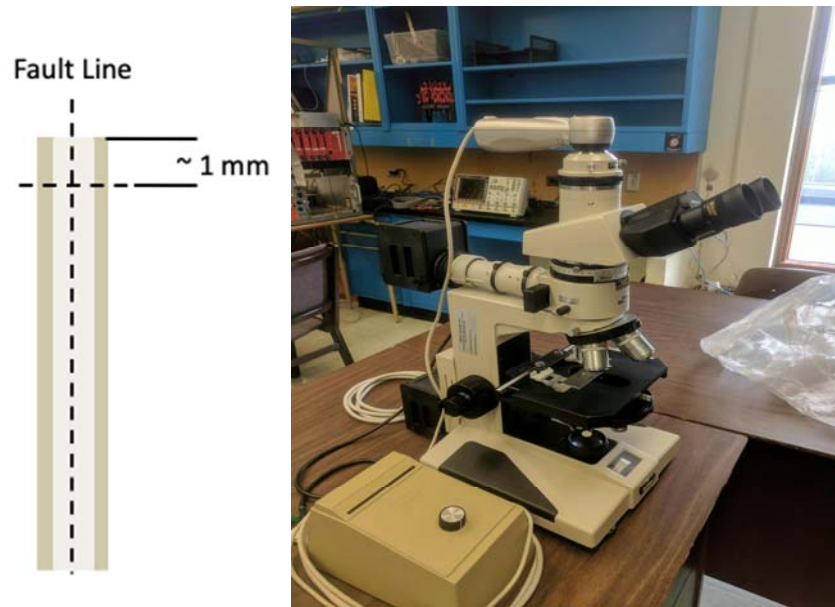


Figure 15: Left, vertical line representing the fault line of the mid-diaphysis cortical tibio-tarsi which was analyzed via SEM and EDS, and the ~1mm section of broken bone which was removed for OM. Right, image of the Nikon Optiphot reflection and transmission microscope used in this study.

2.9 Scanning Electron Microscopy and Energy Dispersive Spectrometry (Bone)

SEM provides a unique advantage over optical microscopy by attaining much greater magnification. Since optical microscopy utilizes visual spectrum photons with wavelengths on the order of hundreds of nanometers, the upper limit of magnification is around 1500x. SEM avoids this limitation by making use of the De Broglie wavelength of the electron [51]. These can be orders of magnitude smaller than what is possible with optical wavelength photons. The electron microscope functions as is depicted in Figure 7, and the procedure is as follows: under vacuum, current is run through a (typically Tungsten) cathode wire, which “boils” off electrons through thermionic emission, at a rate that is dependent upon the magnitude of applied current [53]. These are subsequently accelerated and collimated by an electric field. The electrons are then directed to one-pixel area of the sample, where they interact with the material in question [53]. One such possible interaction of interest is the electron-electron knock-on collision; these set

loose secondary electrons from the K-shells of atoms in the sample at relatively low kinetic energy [53]. Therefore only electrons set loose near the sample surface are likely to find their way to the positively charged detector plate located above the sample, therefore all detected electrons are providing information about the material surface. Electron flux at the detector surface is indicative of the topological information of the pixel area [53]. This beam is then rastered through an area to generate an image. Additionally, secondary electron emission within the sample gives rise to the production of characteristic X-Rays from the electron vacancies that are left behind. These characteristic X-Rays can be detected to obtain elemental concentration information in the surface of the sample; this process being the basis of Energy Dispersive Spectroscopy (EDS) [6, 53].

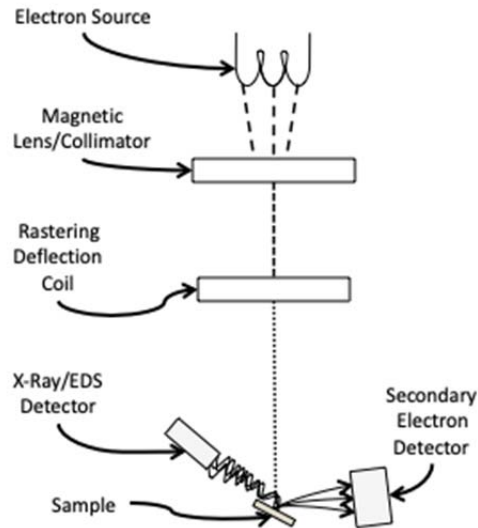


Figure 16: Rough Schematic of a Scanning Electron Microscope equipped with EDS.

A JEOL model 6400 Scanning Electron Microscope, equipped with Energy Dispersive Spectrometry was used to analyze the fault lines in the mid-diaphysis cortical tibio-

tarsi of one sample from each group. Image acquisition parameters are as follows: 30kV-accelerating potential, with 1.0×10^{-11} A beam current.



Figure 17: JEOL model 6400 Scanning Electron Microscope, similar to that used in this study.

2.10 Stone Hardness Testing (Grit)

In order to compare the mechanical efficiency of slag versus pristine gravel as a grit source, two separate hardness tests were conducted on both. These are commonly used in engineering analysis of materials; they are the Brinell and Rockwell hardness tests [7, 8]. Firstly, the Brinell Hardness Test (BHN) in units of kgf/mm^2 , consists of a hydraulic press with a steel indenter tip of known dimensions applying a known force (in units of kgf ; where $1\text{kgf} = 9.8066\text{N}$) to the material in question. After the application of this force, the indentation diameter is measured, see figure 8 [8]. Now, equation 7 can be used to determine the BHN value with all known parameters. Similarly, the Rockwell test uses a hydraulic press, however, this test can be done with a variety of tips, depending on the material in question [7]. In measuring Rockwell Hardness, RH, a primer force is applied to the material. Once

the indenter has settled at a specific depth, additional force is applied, and once again the system is allowed to come to rest. Finally, the additional force is removed, leaving only the primer force, and it is permitted to come to rest, see figure 9 [7]. The difference in penetration depth before and after the additional force is applied gives the value of 'd' to be used in equation 8, along with scaling factors that depend on the type of indenter used, and forces applied [7].

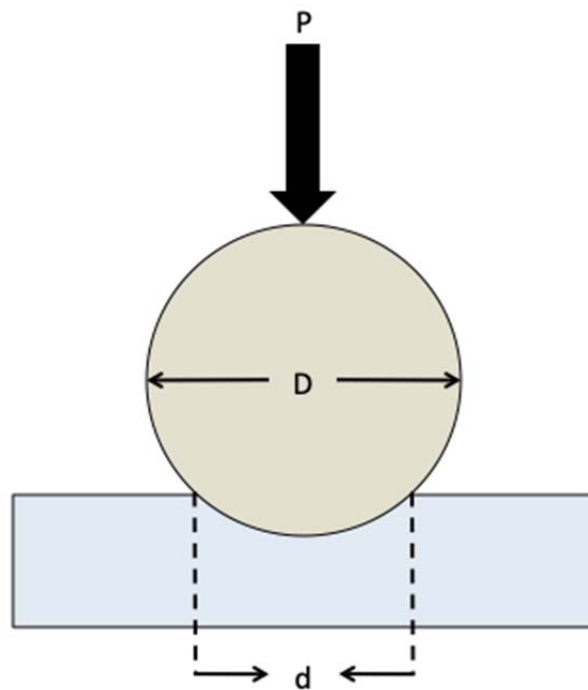


Figure 18: BHN diagram.

Equation 10: Brinell Hardness Number (BHN) equation, where P = applied load (kgf), D = indenter diameter (mm), and d = diameter of indentation (mm).

$$BHN = \frac{2P}{\pi D(D - \sqrt{D^2 - d^2})}$$

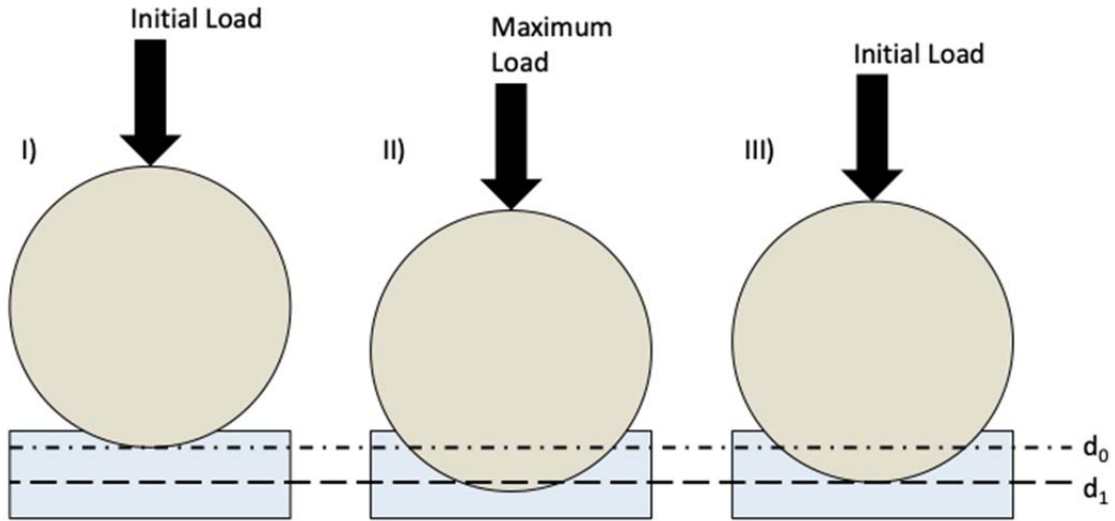


Figure 19: RH Test diagram.

Equation 11: Rockwell Hardness value (RH), where N = scaling factor, $d = d_0 - d_1$ (penetration depth), and s = scaling factor.

$$RH = N - \frac{d}{s}$$



Figure 20: Brinell Hardness testing apparatus (Louis Small Inc. Model 8BLP Brinell Hardness Tester, Cincinnati, OH, USA) used in this study.

2.11 X-Ray Fluorescence (Slag)

To get a radiological perspective of the elemental content of the slag with an emphasis on iron content, X-Ray Fluorescence was used. This is a technique for elemental analysis, which much like EDS exploits the fact that each element of the periodic table, upon ionization, will emit what is known as “Characteristic X-Rays” [6]. These Characteristic X-Rays are emitted when an ionized atom returns to its ground/stable state, by allowing a higher shell (lower binding energy) electron to “fall” into the place of a K-shell (more strongly bound) or lower energy orbital electron that has been displaced via either the photoelectric (Z-dependent), or Compton (Z-independent) effects [6]. These emitted X-Rays are regarded as ‘characteristic’ since their energy is equal to the difference of energy between the start and end point binding energies of the electron that is said to be ‘falling’ into the vacant orbit of the emitted electron. These differences in energy are going to be exclusive to every element, and therefore are “characteristic” of each element [51]. We can then corroborate previous work [1] which showed that iron is a large elemental constituent of this material. It should be noted that there exists a physical effect that competes with the emission of characteristic X-Rays, the Auger effect. In these cases, the emitted energy from the vacancy-filling electron transition is transmitted to an electron from a higher orbital shell which is subsequently ejected from the atom. It follows that the kinetic energy of an Auger electron will be equal to the energy difference from the vacancy-filling transition.

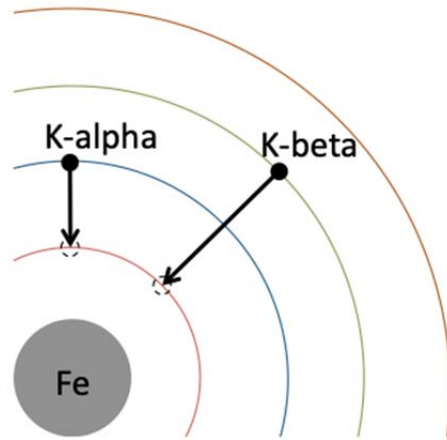


Figure 21: Diagram of iron atom. Electron K-shell depicted in red, L-shell in blue, and M-shell in green. K-alpha and K-beta transitions are indicated.

The detector used in this technique was an intrinsic Germanium cryogenic detector. These consist of a Lithium doped Germanium crystal held at a temperature near that of liquid nitrogen ($\sim 63\text{K}$) to ensure that only electrons that have interacted with a relatively high energy photon will have sufficient energy to enter the conduction energy band [49]. Within the conduction band, the electrons may be susceptible to an electric field that is used to send them and their “holes” (electron vacancies) to their respective cathode or anode, thus generating a signal [49]. If the detector is not maintained at a temperature of roughly 63K , the electrons within the crystal will have a higher probability of jumping the bandgap to the conductive band via thermal effects, causing an excess of noise in the spectral readout.

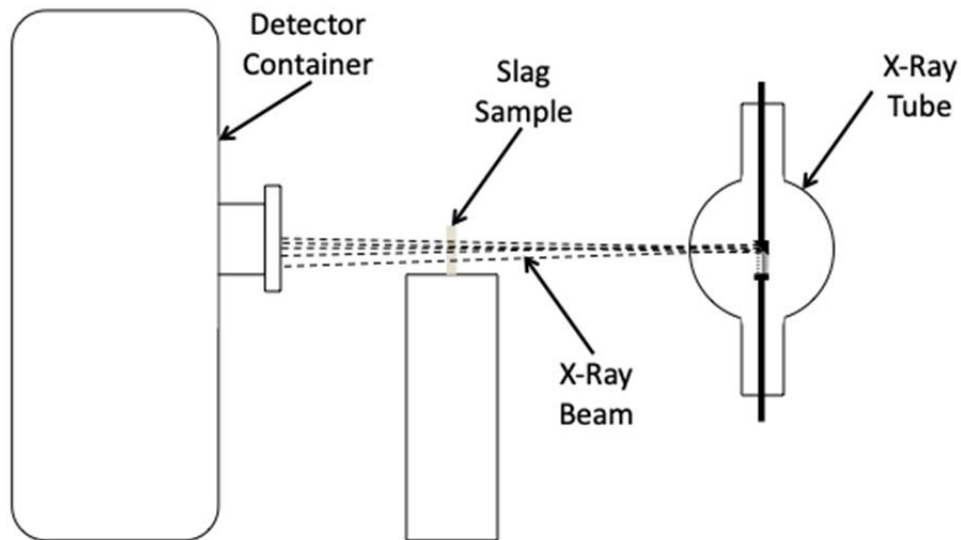


Figure 22: X-Ray fluorescence diagram showing detector, sample, and X-Ray tube.

X-Ray Fluorescence data was acquired only for one sample of slag. Using an X-Ray beam generated from a Toshiba model D-088 dental X-ray tube, operated at 70kVp , and with an applied current of 10mA . The main beam was directed at the sample

and a cryogenic intrinsic Germanium detector detected the reflected x-rays. This allows ionization of the sample and the subsequent emission of characteristic X-Rays; the energy of these X-Rays is then registered and plotted in figure 37.



Figure 23: Image of the X-Ray Fluorescence set-up used in this experiment. The slag sample can be observed at the center of the image (black object on metal cylinder). At the left of the image is located the Intrinsic Cryogenic Germanium Detector.

2.12 Electrothermal Vaporization – Inductively Coupled Plasma – Optical Emission Spectrometry (Bone and Slag)

Additional testing was undertaken with ETV-ICP-OES at Queens University in collaboration with Dr. Dianne Beauchemin, and her graduate student, Margaret MacConnachie. The goal of this additional testing was to quantify any difference in the sulfur content of the bones. The decision to investigate this parameter was made after most of the testing had been completed and after the EDS results showed a roughly 2% by weight sulfur content in the experimental and 0% in the control bone samples. For this reason, we wanted more precise measurements of sulfur content in the entire sample volume (instead of simple surface measurements). Also some additional corroboration with conventional mass spectrometry results and other

trace metal information can also be obtained from this additional testing as these can also influence bone health [43]. ETV-ICP-OES is an ideal method for this type of investigation as next to no sample preparation is required for the analysis and small sample volumes are non-problematic.

This measurement consists of three main steps: ETV, ICP, and OES. The first step is Electro Thermal Vaporization (ETV), the rapid heating and subsequent vaporization of the sample. This is accomplished via deposition of the sample onto an electrothermal probe, which is rapidly heated with an applied current to the device [55]. Next is Inductively Coupled Plasma (ICP), whereby the vaporized sample is injected into superheated plasma, such as argon, causing ionization and characteristic excitation of the sample [54]. This excitation results in the emission of photons of specific wavelengths, which are characteristic of the excited elements. This signal is analyzed in the final part by Optical Emission Spectroscopy (OES). By analyzing the spectrum of characteristic emissions, precise fractional information of constituent elements can be derived [56].

ETV-ICP-OES was performed using a Spectro ARCOS Lateral View ICP-OES and a model ETV 4000-C electrothermal vaporizer. CF_4 reaction gas was added to the ETV furnace to increase volatility of the elements with a flow rate of 0.6 l/min. ICP-OES parameters were set at: plasma RF power of 1.4 kW, Ar flow rate at 12 l/min, and a sampling rate of 10 Hz. Three certified reference materials were used; Durum Wheat Flour (DUWF) was used for external calibration, and method validation was performed with NIST 8433 Corn Bran.

Chapter 3: Statistical Methods

3.1 Welch's T-test

To quantify the significance of the differences between all quantitative parameters of the control and experimental groups, a Welch's T-test was used. This is an expansion of the "Student's T-test", which can account for significant differences in Variance, and the number of measurements between the two groups [23, 24, 27].

3.2 Pearson's Correlation

To analyze correlations, a simple Pearson correlation was used. The Pearson's correlation, r , is fundamentally a tool to test for linearity in a correlation [26]. It is defined as the ratio of the covariance of two sets of variables to the product of their respective variances. This is the standard test to determine the linear correlation between parameters. If a r -value of 0 is obtained, there is no linear correlation between these groups, a r -value of +1 is indicative of a perfect linear relationship, and conversely, a value of -1 is a perfectly linear anti-correlation [26]. A Pearson Distance also derived for all control-experimental correlation pairs. This is distance metric associated with the degree of clustering [28, 29].

Certain parameters were measured using different sets of samples (i.e. sample codes Y 1-7 measured for BS, while Y 1-9 used for Ca). Given that this statistical analysis is dependent upon the comparison of the different parameters of the same samples, the first step of each analysis was to organize the data so that only the common samples from each parametric pairing would be compared. Once

organized, the variance of each parameter must be tabulated using the following equation:

Equation 12: Variance equation, where N is the number of samples measured for the parameter in question, x is the measured value of sample I, and μ is the mean value of this sample set for the parameter in question.

$$Var(x) = \frac{1}{N-1} \sum_{i=1}^N (x_i - \mu)^2$$

Next, the covariance of the two parameters is determined with:

Equation 13: Covariance equation, where y is the second parameter value of sample I, and ν is the mean value of y for the samples in question.

$$Cov(x, y) = \frac{1}{N-1} \sum_{i=1}^N (x_i - \mu)(y_i - \nu)$$

Finally, equation 14 is used to determine the R-value for each pair of samples.

Equation 14: Correlation.

$$R = \frac{Cov(x, y)}{\sqrt{Var(x)Var(y)}}$$

Additionally, to compare the results of Pearson correlations in the control and experimental groups, a Pearson distance is found. A distance metric associated with the degree of “clustering” between two independent sets of bivariate correlations for specific applications in the biological sciences, has been proposed by Fulekar *M.H* [28]. In this analysis, the difference between control and experimental values of the same parametric comparisons is found, e.g.:

$$d_R = |R_C(x, y) - R_E(x, y)|,$$

where the subscripts C and E represent Control and Experimental groups respectively, and x and y are the parameters in question.

3.3 Distance Correlation

The Distance Correlation was employed to identify all correlations, linear or otherwise [32, 33, 34]. A relatively new test introduced by Szekely et al., it is used here as an additional step in determining changes in bivariate correlations between the control and the experimental groups. This parameter can have values ranging from 0 to 1, with 0 indicating a perfect lack of correlation, i.e. complete independence between parameters [50]. On the other hand, a value of 1 indicates perfect correlation, to understand the nature of this correlation (i.e. linear, exponential, etc.), additional analysis is required [50]. This novel statistical metric is used by a number of groups in a variety of applications [35, 36, 37]. An associated distance correlation distance is also found for all control-experimental pairings [50]. This test, introduced by Szekely et al. in 2007 is conceptually similar to the Pearson's Correlation; as such the same pairwise groups are compared, and the same samples within these groups are used to do so. Unlike in the Pearson correlation, the difference is found for parameter 'x', data point 'j' and data point 'k', where 'j', and 'k' range from 1 to n, and signify the samples in question. Therefore the 'distance' between each data point and all other points of data of that parameter is found. It follows then that if 'j' = 'k', then the distance is equal to zero. This generates an n-by-n hollow-symmetric matrix, where the axes of the matrix are representative of the samples of this parameter, for which the matrix elements are the distance (see Figure 24). Once this matrix is generated, the following equations are used to 're-center' or 'normalize' all the data for comparison:

Equation 15: Distance between sample j and sample k of parameter x.

$$a_{j,k} = ||x_j - x_k||$$

Equation 16: 'j' data centering equation. Equivalent to the mean distance for sample 'j'.

$$\bar{a}_j = \frac{1}{N} \sum_{k=1}^N a_{j,k}$$

Equation 17: Parametric centering equation. Equivalent to mean distance for all data points of parameter 'x'.

$$\bar{a} = \frac{1}{N} \sum_{k=1}^N \sum_{j=1}^N a_{j,k}$$

Equation 18: Full centering/normalization.

$$A_{j,k} = a_{j,k} - \bar{a}_j - \bar{a}_k + \bar{a}$$

The re-centering of the data is required to ensure that the distances in both parameters are henceforth comparable. From here, the variances of the two re-centered datasets (dVar) are determined, as well as their covariance (dCov). Finally, the Distance Correlation Value is found with equation 21.

Equation 19: Distance variance.

$$dVar = \sqrt{\frac{1}{N^2} \sum_{i,k=1}^N (A_{j,k})^2}$$

Equation 20: Distance covariance.

$$dCov = \sqrt{\frac{1}{N^2} \sum_{i,k=1}^N (A_{j,k})(B_{j,k})}$$

Equation 21: Distance correlation.

$$\mathfrak{R} = \frac{dCov(x, y)}{\sqrt{dVar(x)dVar(y)}}$$

	x_1	x_2	x_3	x_4	x_5	x_6	...	x_n
x_1	$ x_1 - x_1 $	$ x_1 - x_2 $	$ x_1 - x_3 $	$ x_1 - x_4 $	$ x_1 - x_5 $	$ x_1 - x_6 $
x_2	$ x_1 - x_2 $	$ x_2 - x_2 $	$ x_2 - x_3 $	$ x_2 - x_4 $	$ x_2 - x_5 $	$ x_2 - x_6 $
x_3	$ x_1 - x_3 $	$ x_2 - x_3 $	$ x_3 - x_3 $	$ x_3 - x_4 $	$ x_3 - x_5 $	$ x_3 - x_6 $
x_4	$ x_1 - x_4 $	$ x_2 - x_4 $	$ x_3 - x_4 $	$ x_4 - x_4 $	$ x_4 - x_5 $	$ x_4 - x_6 $
x_5	$ x_1 - x_5 $	$ x_2 - x_5 $	$ x_3 - x_5 $	$ x_4 - x_5 $	$ x_5 - x_5 $	$ x_5 - x_6 $
x_6	$ x_1 - x_6 $	$ x_2 - x_6 $	$ x_3 - x_6 $	$ x_4 - x_6 $	$ x_5 - x_6 $	$ x_6 - x_6 $
...
x_n	$ x_n - x_n $

Figure 24: Depiction of distance matrix, where x is some parameter, and the subscripts 1 through n indicate the sample number.

Analogous to the Pearson distance $d_{x,y}$, we propose the concept of the Distance correlation distance d_R , such that:

Equation 22: Distance Correlation distance.

$$d_R = |R_1 - R_2|$$

Where R_1 and R_2 are the Distance correlations for the first and second data set respectively (control and experimental). Note that equation 23 indicates that the value of d_R must be between 0 and 1.

Equation 23: Limits of the Distance Correlation distance.

$$0 \leq d_R \leq 1$$

We propose a condition of $d_R \geq 0.20$ for statistical “significance” given that we have only one such parametric bivariate that meets this criterion.

Chapter 4: Results and Discussion

4.1 Quantitative Parameters

All quantitative measurement values are presented as mean \pm standard error. All these parameters were subjected to a one-tailed Welch's t-test. This method was used to account for unequal sample sizes and unequal variances between control and experimental groups for the same parameters. A statistical signal to noise ratio was also determined for discussion, this signal to noise ratio is defined as the ratio of the mean to the standard deviation of a data set. Six of seven of the parameters met the commonly accepted threshold for the statistical significance coefficient: $p \leq 0.05$. These results are found in table 1. YM is the only outlying quantitative parameter, remaining just outside the threshold at $p = 0.0662$.

Table 1: Table of quantitative results, with number of sample measurements, and one-tail Welch's t-test values.

	Control	Experimental	p (one-tail)
TH (mm)	0.61 \pm 0.074 (n = 6)	0.48 \pm 0.03 (n = 6)	0.0500
CD (g/cm ³)	1.9785 \pm 0.1948 (n = 9)	1.7698 \pm 0.2223 (n = 9)	0.0251
BMD (g/cm ²)	0.152 \pm 0.005 (n = 6)	0.143 \pm 0.005 (n = 6)	0.0089
	82621.8 \pm 11046.7 (n =	70912.8 \pm 11952.7 (n =	
Ca (ppm)	9)	9)	0.0272
Fe (ppm)	80.87 \pm 37.41 (n = 9)	242.76 \pm 190.35 (n = 9)	0.0127

BS (N)	451.57 ± 133.78 (n = 7)	328.50 ± 139.62 (n = 8)	0.0500
YM (MPa)	3483.6 ± 1853.7 (n = 7)	2835.9 ± 879.6 (n = 8)	0.0662

The mean cortical bone thickness (TH) for the experimental and control groups (both n = 6) were 0.48 ± 0.03 mm and 0.61 ± 0.07 mm ($p = 0.0500$) respectively, representing an approximate reduction in mean thickness of 21% for the experimental group. This loss suggests that slag ingestion is associated with impaired bone development in the relatively young pigeon subjects, consistent with previously reported results by Tsay et al. and De Vernejoul et al., in iron-overloaded murine and porcine models [9,10].

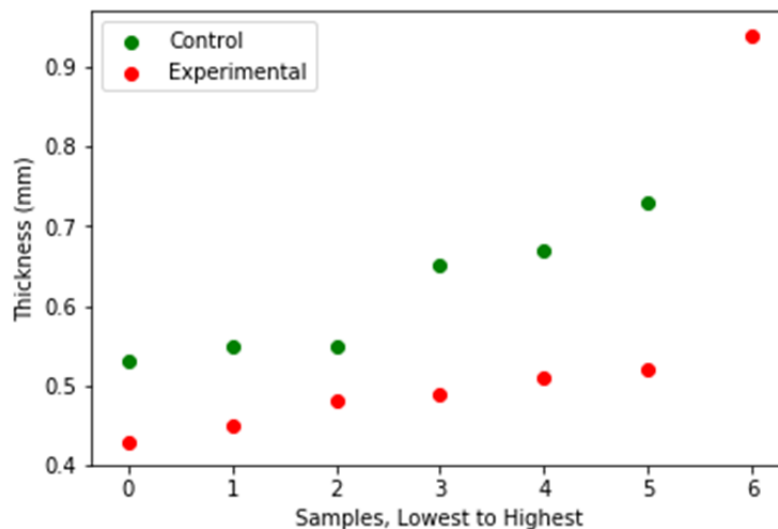


Figure 25: Results from Thickness measurements plotted from lowest to highest for comparison with experimental results in red and control in green.

The mean conventional density (CD) for the experimental and control groups (both n = 9) were 1.7698 ± 0.2223 g/cm³ and 1.9785 ± 0.1948 gm/cm³ ($p = 0.0251$) respectively, representing an approximate difference in mean density of 10% for the

experimental group. These results are compatible with iron overload-induced loss of bone mineral content reported in avian and porcine models [10-14]. To further substantiate iron overload in bone, we later present optical microscopy and mass spectrometric evidence of the presence of an abnormally localized iron deposit in bone in an experimental group sample. No previous reports of decreased bone density in slag fed animals were found in the literature.

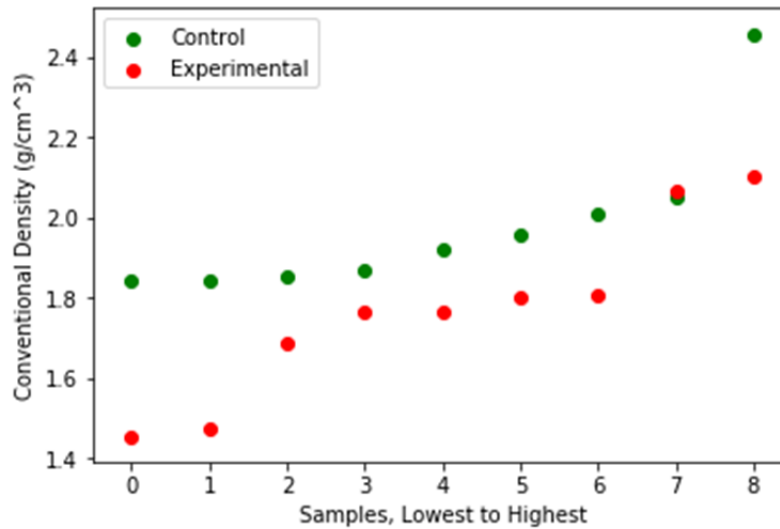


Figure 26: Results from Conventional Density measurements plotted from lowest to highest for comparison with experimental results in red and control in green.

The mean bone mineral density (BMD) for the experimental and control groups (both $n = 6$) were 0.143 ± 0.005 g/cm² and 0.152 ± 0.005 g/cm² ($p = 0.0089$) respectively, representing an approximate loss in mean density of 6% for the experimental group. Relatively elevated data signal to noise ratios of 3289 and 2624 for the control group and experimental groups respectively, resulted in a highly significant difference (p -value of 0.0089). These results are consistent with those of Ward and collaborators, who reported a reduction in BMD, associated with

increased Fe levels in birds [15]. Conrad et al. and later Hester et al., reported a correlation between reduced BMD values in poultry femora, with associated osteoporotic-like conditions [16,17]. In humans, a reduced BMD is strongly correlated with clinical osteoporosis [18]. Furthermore, Kim and collaborators have reported that in humans, iron overload (elevated serum ferritin levels) is associated with reduced BMD levels [19].

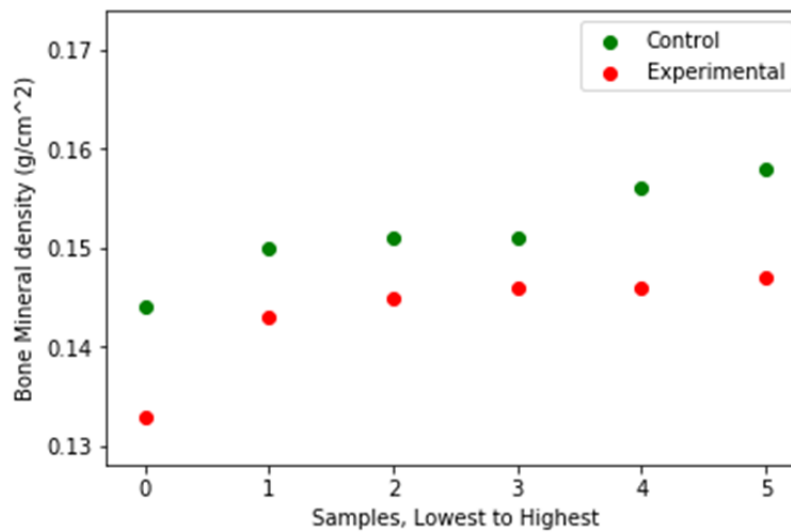


Figure 27: Results from Bone Mineral Density measurements plotted from lowest to highest for comparison with experimental results in red and control in green.

The mean Ca concentrations measured by MS for the experimental and control groups (both $n = 9$) were 70912.8 ± 11952.7 ppm and 82621.8 ± 11046.7 ppm ($p = 0.0272$), representing an approximate loss of 14% of calcium content for the experimental group. This loss suggests that dietary slag (i.e. iron) is associated with reduced Ca uptake/retention in bone, which will be discussed later.

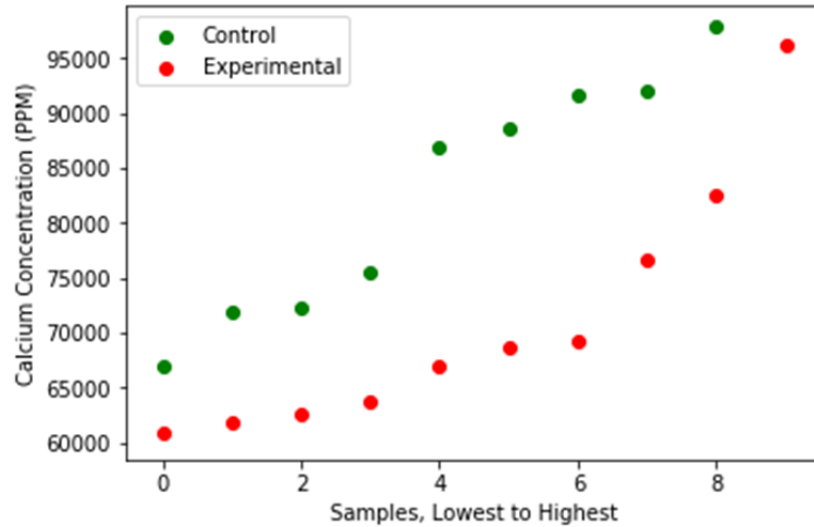


Figure 28: Results from Calcium Concentration measurements plotted from lowest to highest for comparison with experimental results in red and control in green.

The mean Fe concentration measurements reveal a remarkable difference between groups: 242.76 ± 190.35 ppm for the experimental group, and 80.87 ± 37.41 ppm for the control group (both $n = 9$, $p = 0.0127$). This represents about a 200% increase in Fe concentration in the experimental group. The large error interval for the experimental group is possibly associated with the non-homogeneous deposition of iron in the samples combined with the sample preparation procedures in which only 0.5g of the average ~ 2 g of bone was analyzed. The idea of non-homogenous iron deposition is supported by optical microscopy results and Energy Dispersive Spectroscopy (EDS) measurements. Inverse correlations between bone calcium content and iron overload in animal models have been reported in the literature. For example, Tsay et al. reported an inverse correlation between iron overload and bone calcium content in mice [9]. Likewise, Vernejoul and collaborators described alterations in bony calcium metabolism in porcines subjected to iron overload [10].

Dorrestein et al. reported elevated Fe levels in bones in pigeons fed a high Fe concentration diet, but did not address any changes in Ca concentrations [20].

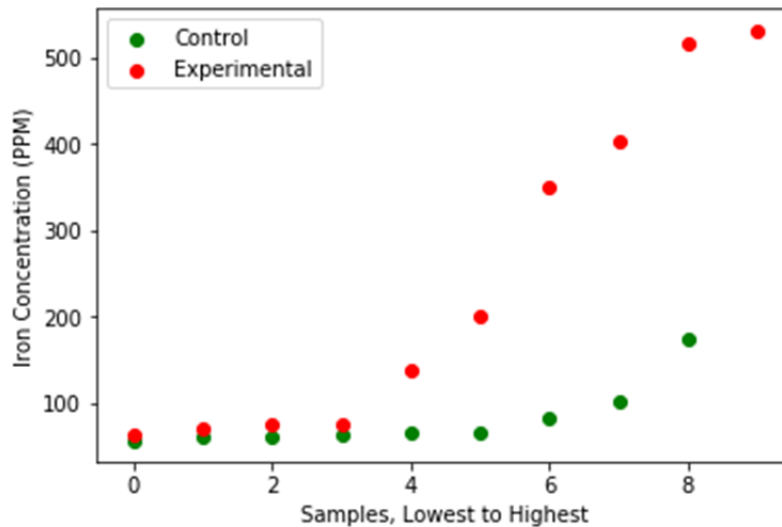


Figure 29: Results from Iron Concentration measurements plotted from lowest to highest for comparison with experimental results in red and control in green.

The mean breaking strength (BS) values for the control and experimental groups ($n = 7$ and $n = 8$ respectively) were 451.57 ± 133.78 N and 328.50 ± 139.62 N ($p = 0.0500$) respectively, representing an approximate reduction of 27% for the experimental group. Kim and collaborators have reported BS measurements in poultry bones; however, they did not examine samples with modified diets [3]. In work that has some similarities to our own, Huyghebaert and collaborators investigated the effects of dietary fluoride on the breaking strength of the leg bones in broiler hens [21]. From a structural point of view, this reduction in breaking strength is consistent with our cortical thickness (TH) measurements mentioned earlier, where we report a 21% reduction in the mean thickness of the experimental group. Zhang and collaborators have reported comparable results in hen bones, in which a reduction in BS was associated with reduced bone dimensions [22].

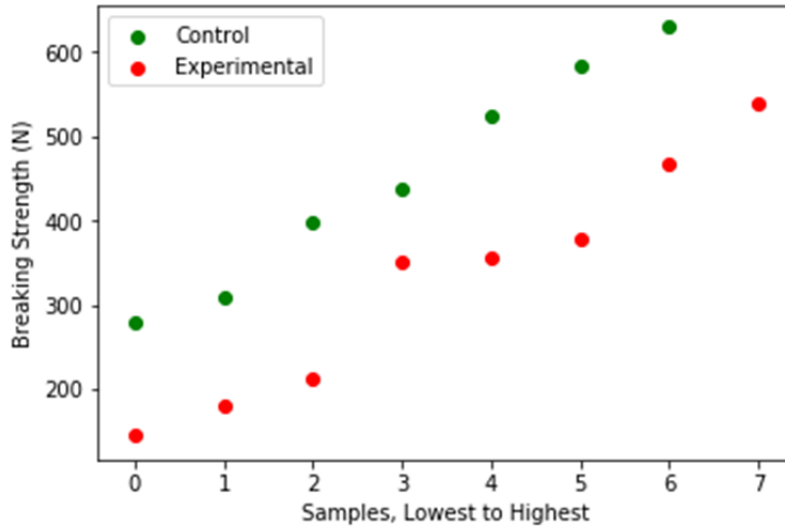


Figure 30: Results from Breaking Strength measurements plotted from lowest to highest for comparison with experimental results in red and control in green.

The mean Young's Moduli (YM) values for the control and experimental groups ($n = 7$ and $n = 8$ respectively) were $3483.6 \pm 1853.7\text{MPa}$ and $2835.9 \pm 879.6\text{MPa}$ ($p = 0.0662$) respectively, representing an approximate reduction of 19% in the YM of the experimental group. Due to a large dispersion in the control group data, this result did not meet the $p \leq 0.05$ criteria associated with statistical significance [23,24]. Table 1 presents the results of the seven parameters measured for both the control and experimental groups, with the relevant sample numbers and confidence levels. In figure 32, histograms (including errors) summarizing the complete quantitative data set in relative terms are presented. The bars are normalized such that the controls' mean value is set to unity (with the exception of Fe concentration, where the experimental mean is set to unity instead, to avoid geometric scaling complications). The data from YM measurement is plotted in figure 31, and it becomes clear that although there is a fair amount of separation between the

control and experimental data, there is also far more overlap than in any other dataset.

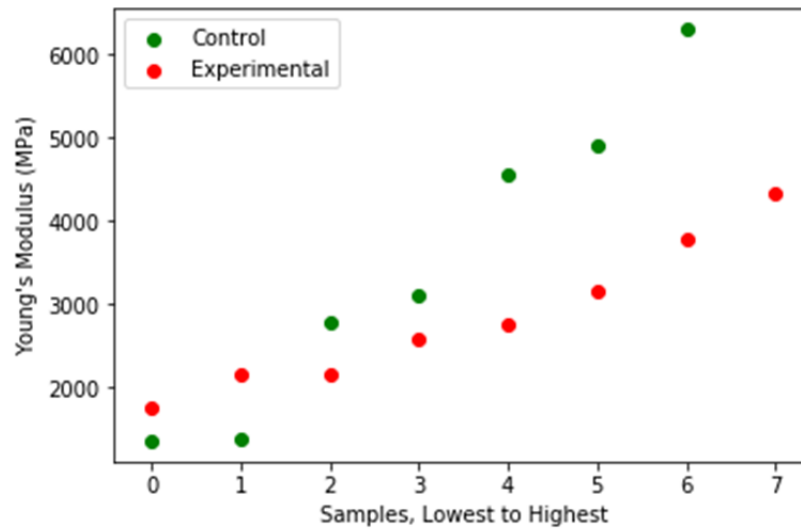


Figure 31: Results from Young's Modulus measurements plotted from lowest to highest for comparison with experimental results in red and control in green.

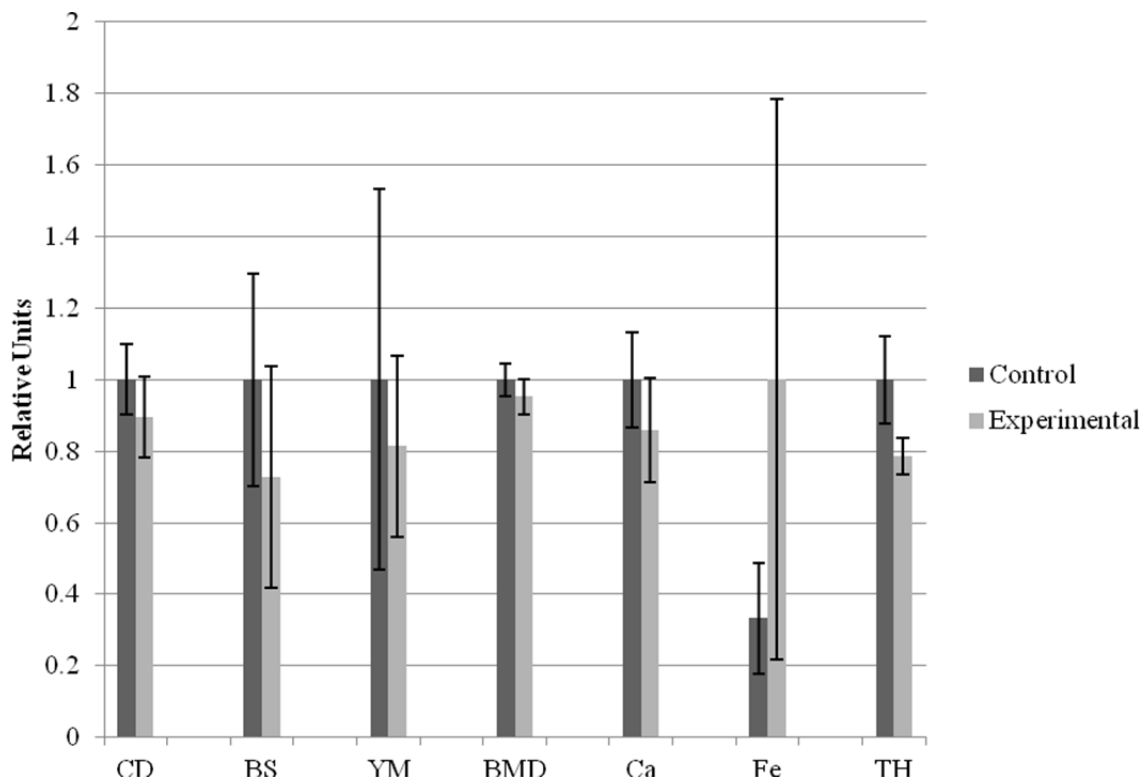


Figure 32: Histogram depicting the full quantitative data set in relative units with relative error bars. The control group set to unity for all but Fe.

The preliminary results from ETV-ICP-OES are shown in table 2. These results are generally compatible with those obtained through conventional mass spectrometry for the relative iron and calcium concentrations. Additional interest arises from the increased (two-fold) concentration in aluminium in the experimental group, which had not been previously considered. A lower concentration of sulfur is observed in the experimental group, however it should be noted that the difference in measurement between the two groups is within uncertainties, therefore a hard conclusion cannot be obtained.

Table 2: Preliminary ETV-ICP-OES results, results are shown with standard deviation.

Element	Slag (%, n=5)	Control (mg/kg, n=5)	Experimental (mg/kg, n=5)
Al	2.48±0.67	6.5±2.4	12.3±2.0
Ca	6.5±1.3	78200±16000	45097±11000
Fe	5.8±1.8	38±13	51±14
Mg	4.1±2.1	2550±590	2355±510
S	0.74±0.15	3618±730	2950±650

Figure 33 shows the analysis that identifies the significant results from the data. From this bar graph we can conclude that the aluminium and calcium concentration measures have a difference greater than the standard deviations of the data. Iron and sulfur concentration measures have standard deviations that are comparable to the difference in the means, and as such would not meet the criteria of statistical significance via Welch's t-test.

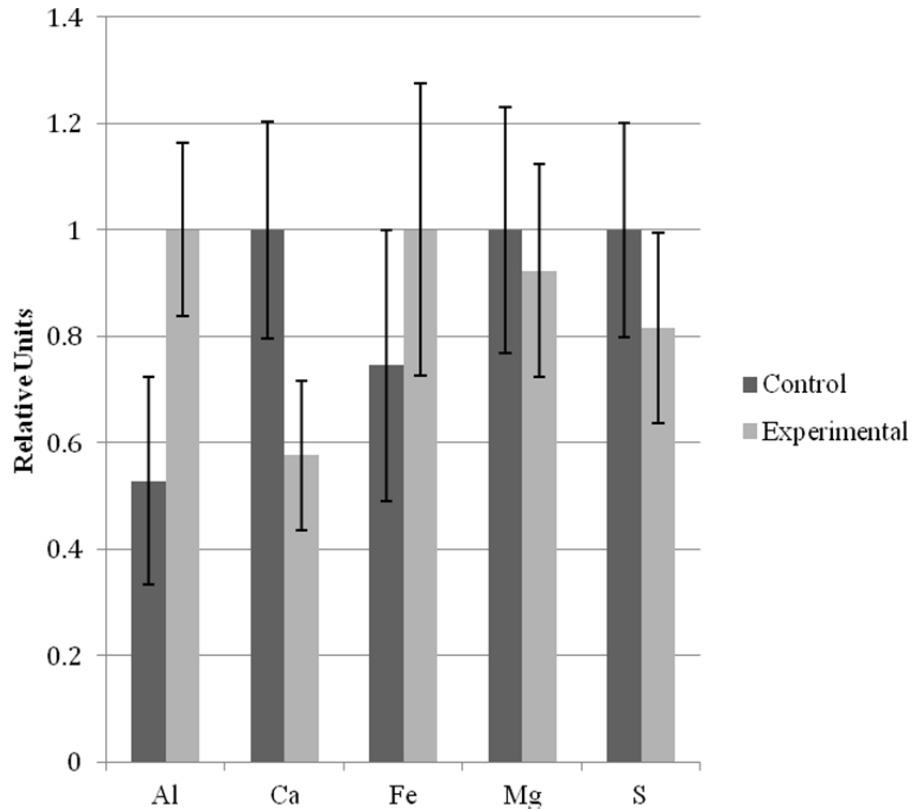


Figure 33: All ETV-ICP-OES results shown in relative units to compare control samples with experimental.

4.2 Qualitative (and semiquantitative) Parameters

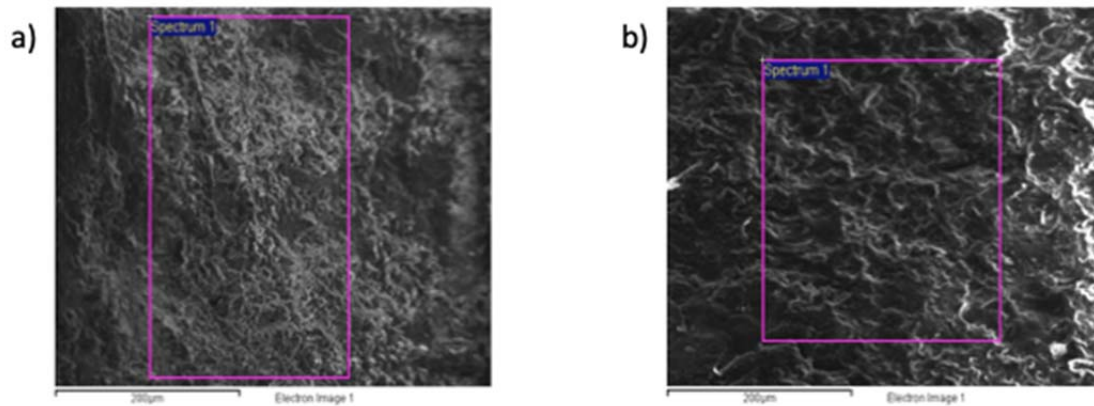


Figure 34: a) Electron micrograph of representative control sample. B) Electron micrograph of representative experimental sample with visible cavitations and loss of the granular architecture that is clearly visible in a).

Table 3: Mean EDS results, standard deviations are omitted given the small sample size (n=2) and as these results are provided for comparison with ETV-ICP-OES results.

Element	Control (%, n=2)	Experimenta l (%, n=2)
O	70.74	82.11
P	13.96	7.88
S	0	2.66
Ca	15.31	7.35

Electron micrographs of cortical tibio-tarsi of a representative sample from the control group (normal diet) on left, and experimental group (slag diet) on right are presented in figures 34a and 34b respectively. The loss of granular architecture in the experimental sample is consistent with an increase in bone resorption. In particular, the typically larger cavities observed are consistent with resorptive cavities lined with osteoclasts. The observed changes may also be indicative of cortical discontinuities, foci of woven bone formation, and/or spicules of fibroplasia, consistent with previously reported histological findings [1]. Brissot et al. described generally similar changes in bony structures in humans subjected to iron overload conditions [25]. Although not directly relevant to this work, for purposes of completeness we mention the work of Conrad et al. who addressed soft tissue changes induced by iron overload in humans [16]. Follow-up EDS analysis (areas inside the rectangles) revealed the presence of elemental sulfur at a concentration of $2.66 \pm 0.02\%$ by mass fraction in the experimental sample, with no sulfur

detected in the control sample as seen in table 3. This correlates well with the reported $2.5 \pm 0.5\%$ sulfur concentration by mass in nickel recovery slag in the Sudbury basin as reported by Galiano and Lapointe, 2019 [2, 29]. It is noted that the EDS results for sulfur content do not match with the preliminary ETV-ICP-OES, perhaps a result of the small sample size for EDS.

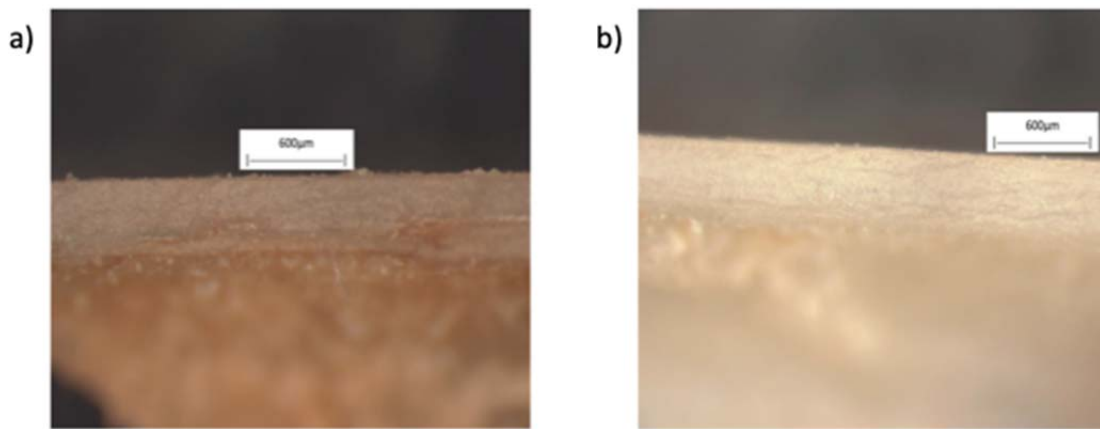


Figure 35: a) Optical micrograph of representative experimental sample along a fault after UTM testing. Note the brown coloring, which may be the result of higher iron content, and the frayed edges along the periosteum and endosteum. B) Optical micrograph of representative control bone along fault line after UTM testing. Note here the milky white color and sharp edges along the periosteum and endosteum.

Figures 35a and 35b are section optical micrographs of cortical tibiotarsi of the control group sample (normal diet) on left, and experimental group sample (slag diet) on right. The micrographs reveal a thinning of the cortical thickness of the experimental sample, from approximately $600\mu\text{m}$ to $500\mu\text{m}$, for an approximate 15% reduction in thickness. The periosteal and endosteal borders appear irregular and discontinuous in the experimental sample, with protuberances in the periosteum and indentations in the endosteum, consistent with increased resorption. None of these abnormalities are apparent in the control sample, which presents with smooth periosteal and endosteal surfaces.

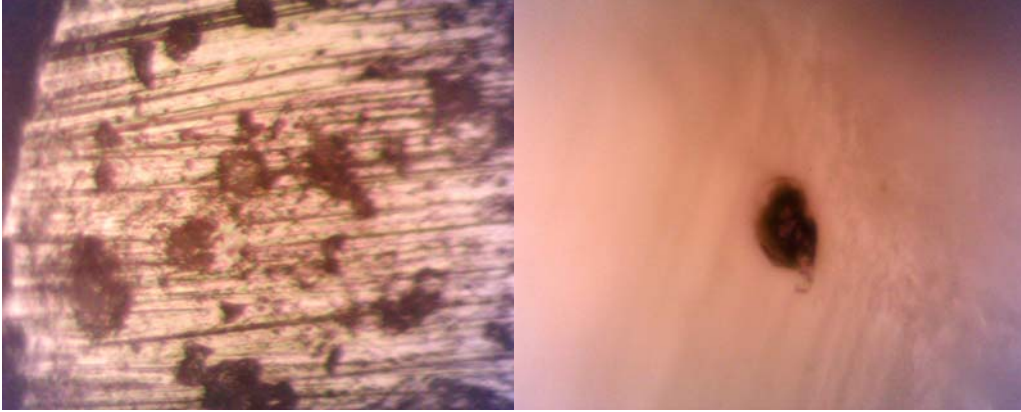


Figure 36: Optical micrographs of experimental samples. On the left, notice parallel-arranged spicules and cavities. On the right, a red-brown localized circular deposit, approximately 40 μ m in diameter, many of which were found in experimental samples, none in control.

Further conventional microscopy analysis of the experimental samples revealed the presence of ovoid-shaped granular cavities, ranging in diameter between 50 μ m and 200 μ m. These cavities were surrounded by parallel-arranged spicules, as presented in figure 36. The cavities contain increased quantities of osteoclasts, in effect constituting resorptive cavities, compatible with the electron microscopy findings. The spicular structures appear to be areas with an overrepresentation of osteoblasts and/or fibroblastic changes; however, further investigation is needed to confirm this. No such structures were observed in the control samples.

Optical microscopy at the highest available magnification (1500x), revealed the existence of a red-brown localized circular deposit – of approximately 40 μ m diameter – on the cortical structure of the experimental sample, as seen in figure 36. On follow-up EDS analysis of the specific spot, an approximately eightfold increase in Fe concentration (by mass fraction) was found relative to the surrounding cortical bone. The mean Fe mass fraction within the area of the spot was $0.22 \pm 0.01\%$, compared to a mean value of $0.026 \pm 0.001\%$ for the surrounding bone. Considering that our MS measurements have shown a three-fold increase in (mean)

Fe concentration in the experimental samples, this additional EDS result implies that the localized deposit exhibits a 24-fold increase in Fe concentration compared to the mean values for the control group. Based on abnormally high Fe concentrations reported in the liver and kidneys of these very same laboratory animals, a condition of hemosiderosis had been proposed [1]. Previous reports of avian hemosiderosis exist, but none specifically addressed Fe concentrations in bones [11,12]. This is believed to be the first report of a localized deposit of abnormally high Fe concentration in bone in an avian sample with known hemosiderosis. No such deposits were observed in our control samples, despite determined efforts to identify them.

The last part of our investigation involved hardness measurements of the dietary components of the two groups. Brinell testing yielded a mean number of 81.2 (n = 3) for slag and 35.4 (n = 4) for limestone, while Rockwell testing yielded numbers of 634 and 327 (both n = 1), for slag and limestone respectively. An approximate hardness ratio of 2:1 for slag vs. limestone was supported by both independent testing methods yielding a robust conclusion in this case. The greater mechanical hardness of slag very likely played a role in its well-documented slower rate of in-vivo erosion, and greater retention time in the gastric system [1].

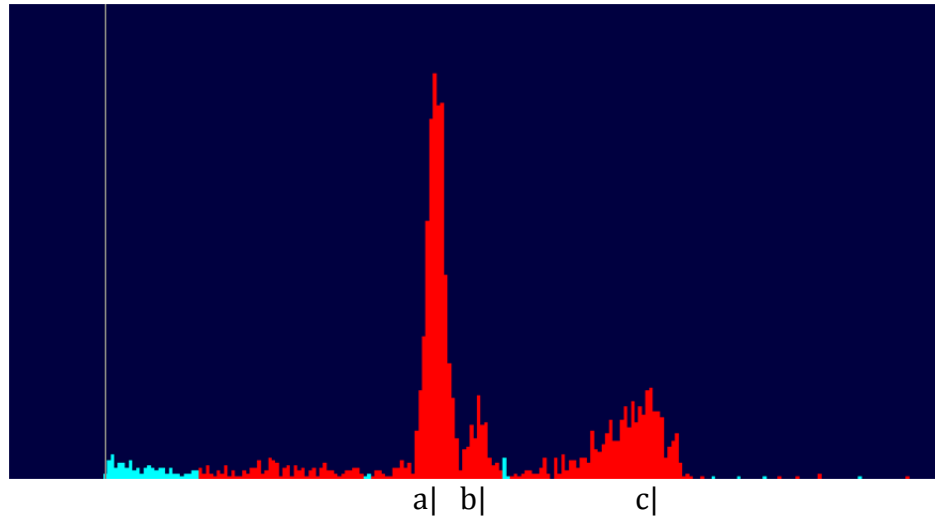


Figure 37: Energy spectrum from X-Ray Fluorescence of slag acquired with intrinsic Germanium cryogenic detector. a) Peak of the 6.4keV K-alpha characteristic emission from iron fluorescence. b) Peak of the 6.9keV K-beta characteristic emission from iron fluorescence. c) Energy spectrum resulting from Compton Scattering within the detector.

X-Ray Fluorescence on a slag sample yielded the graph from figure 37. Here we can see the peaks at a) and b) indicating the K-alpha (6.4keV) and K-beta (6.9keV) characteristic X-Ray emission energies of iron. These are the only pronounced peaks visible in the plot besides the small normal distribution at c) caused by Compton scattering within the detector at the higher energy end of the graph. The peaks at these characteristic energy levels are indicative of a great presence of iron.

4.3 Pearson Correlations

All Pearson correlation results for control, and experimental groups can be found in tables 4 and 5 respectively. A threshold of significance of $R > 0.70$ based on the suggestion of Fulekar et al. was used for all correlations. Additionally, Pearson Distance values are found in table 6.

Table 4: Pearson correlation values for all control parameters.

R _C	Fe	Ca	YM	BS	CD	BMD
Th	-0.616	0.7623	-0.4604	-0.8998	-0.4086	0.7131
BMD	-0.2393	0.2117	0.2511	-0.137	-0.7895	-
CD	0.0929	0.4202	-0.0699	-0.0004	-	-
BS	0.4316	-0.3955	0.7431	-	-	-
YM	-0.0403	-0.0136	-	-	-	-
Ca	0.38	-	-	-	-	-

Table 5: Pearson correlation values for all experimental parameters.

R _E	Fe	Ca	YM	BS	CD	BMD
Th	-0.353	0.0791	0.2929	0.3988	-0.3877	-0.9018
BMD	-0.0206	0.1801	0.0611	0.8732	0.8497	-
CD	-0.262	0.106	-0.1327	0.0218	-	-
BS	-0.5464	-0.3141	0.5286	-	-	-
YM	-0.7875	-0.6715	-	-	-	-
Ca	0.58	-	-	-	-	-

Table 6: Pearson distance values for all parameters.

d _R	Fe	Ca	YM	BS	CD	BMD
Th	0.263	0.6832	0.7533	1.2986	0.0209	1.6149
BMD	0.2187	0.0316	0.19	1.0102	1.6392	-
CD	0.3549	0.3142	0.0628	0.0222	-	-
BS	0.978	0.0814	0.2145	-	-	-
YM	0.7472	0.6579	-	-	-	-
Ca	0.2	-	-	-	-	-

Significance was found in the following control sets: Ca-TH, BS-TH, BMD-TH, and YM-BS. These significant correlations can be explained as follows: -First, thicker bones are likely to consist of a larger fraction of calcium hydroxyapatite (the structural molecule of the bony matrix) to collagen/soft matter, hence Ca-TH $p = 0.7623$. BMD-TH, $p = 0.7131$, since the BMD scan is a two-dimensional measure of density, with units of g/cm^2 of a three-dimensional object, it is reasonable that a thicker object will produce a higher BMD value. -Secondly, YM-BS strongly correlated with a $R = 0.7431$ since YM is calculated concurrently with BS, what is unexpected however is the relative lack of correlation between YM-TH, as YM also is

dependent on the value of TH. A rather unintuitive strong anti-correlation between BS and TH was observed in this group; this anticorrelation will need to be further explored.

Significant correlations in the experimental group are the following: BMD-TH, BS-BMD, CD-BMD, and Fe-YM. First, the BMD-TH correlation just as in the control group is found to be significant, however in the inverse direction as $R = -0.9018$. This is indicative of lower calcium concentration (Bone Mineral Density) in the thicker experimental bones, conversely, no such correlation was observed between Ca and TH. In accordance with reported results [18], BS-BMD is found to correlate strongly with a $R = 0.8732$; this correlation is not observed in the control group. Next, CD-BMD has an $R = 0.8497$. This result can be explained if one considers that a sample with a higher concentration of high atomic number elements will have higher density. This particular result may be due to the generally higher iron concentration, however, no significant correlation between Fe-CD was found. The final result of significance in the experimental group is the Fe-YM at $R = -0.7875$. This may be indicative of a change in the mechanical properties of the bones with a higher concentration of iron. Specifically, high Fe relates to lower YM, that is, “softer” bone. No such relationship was found in the control group, a further indication that there is a threshold of Fe that must be reached before changes are observed.

Pearson Distances between both groups for all parameters can be found in table 6. For this metric, a threshold of significance of $d \geq 1.0$ is used, as suggested by Fulekar. By this criterion, significant distances are observed for the following pairs of bivariate relationships: BS-TH, BMD-TH, BS-BMD, CD-BMD.

Starting with Ca-TH, there is a considerable drop in the significance from the control to the experimental group. From this, we can infer that the dietary modification from slag grit negatively impacts the relationship between Ca and TH. We see that TH, and Ca of the experimental group samples were significantly lower than that of the control group; therefore it may be conceived that the modified diet has resulted in a shift in the ratio of calcium hydroxyapatite, and bone thickness/bone mass. This argument is further supported by BMD-TH $d = 1.6149$, where a strong positive correlation is observed in the control and strong negative correlation in the experimental group.

For BS-TH, $d = 1.2985$: this is a rather large change from the unexpected strong negative correlation in the control group to a slight (but not significant) positive correlation in the experimental group bivariate.

For BMD-TH, $d = 1.6149$, which as discussed above in the Ca-TH section, is very likely indicative of a physiological change in the formation of bone matrix, in which the ratio of soft tissue (or bone collagen in this case) to bone mineral is greatly impacted.

For BS-BMD, $d = 1.0102$, which indicates a nearly complete independence in the control group to a strong correlation in the experimental group. This can be considered indicative of a threshold below which BMD must fall before an impact on BS can be observed.

For CD-BMD, $d = 1.6392$, which indicates a strong negative correlation in the control to a strong positive correlation in the experimental group. Once again we can thus infer a change in the physiology of bone development and bone structure. It is

evident that the more dense control bone is likely to have lower mineral content, whereas the denser experimental bone samples are likely to have more mineral content, in particular, the relatively heavier iron.

4.4 Distance Correlation

Distance correlation values for control and experimental can be found in tables 7 and 8 respectively. Notable results here can be compared to the results of section 3.3 to infer non-linear relationships that might be missed by the Pearson correlation. Significance will be granted to values of 0.95 or above for this metric, as recommended by Kong et al. [33]. This is a stricter threshold of significance than that used in the Pearson correlation; this is to compensate for the fact that the distance correlation is more sensitive to statistical noise. I.e. the inclusion of linear correlations described by R as well as non-linear relationships, where perhaps none exist.

Table 9 contains the Distance Correlation distance (d_R), which is the distance correlations analog of the Pearson distance. This is a new metric introduced by Lapointe and Galiano (2020). For this metric, a threshold of significance of 0.2 is chosen as reported in Lapointe, Galiano (2020) [50]. As such, BMD-Ca is the only bivariation to meet this criterion. It is observed that in the control group, a Distance correlation of 0.9 is observed, this does not quite reach the threshold of significance, however it is still a relatively high value. The experimental Distance Correlation value for this bivariation is a mere 0.68, well outside the threshold of significance.

Table 7: Distance correlations for control group.

R_C	Fe	Ca	YM	BS	CD	BMD
Th	0.83	0.92	0.82	0.95	0.88	0.86
BMD	0.66	0.9	0.93	0.86	0.88	-
CD	0.73	0.83	0.85	0.85	-	-
BS	0.76	0.85	0.94	-	-	-
YM	0.71	0.89	-	-	-	-
Ca	0.84	-	-	-	-	-

The only significant control group relationship then, is the BS-TH relationship. This is evidence of the Distance Correlations ability to identify linear relationships just as the Pearson Correlation. This is evident as the Pearson Correlation of this same bivariation is $R_C = -0.89$. It is also noted that there may be a relationship between the Pearson Correlation and Distance Correlation for bivariate pairs with linear significance, as determined via the Pearson Correlation. More on that point later.

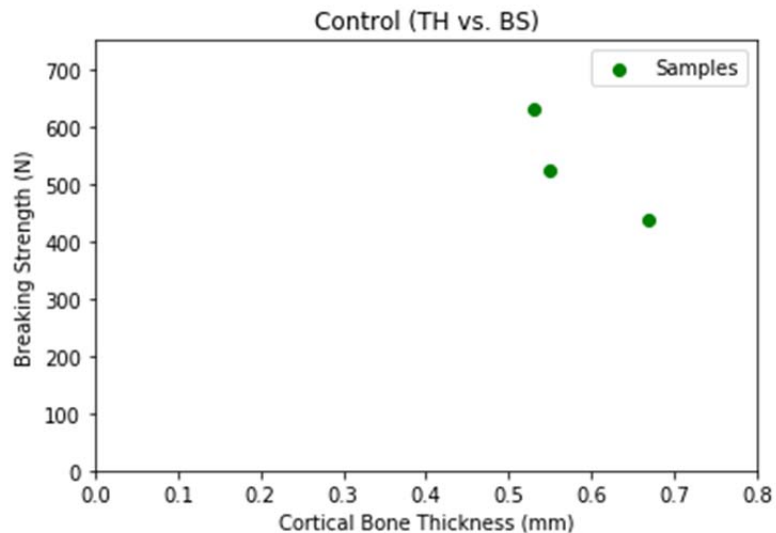


Figure 38: Despite the low number of measurements for this bivariate comparison ($n=3$), a linear relationship is observed.

Table 8: Distance correlations for experimental group.

R_E	Fe	Ca	YM	BS	CD	BMD
Th	0.85	0.75	0.93	0.89	0.86	0.94
BMD	0.69	0.68	0.74	0.94	0.9	-
CD	0.77	0.71	0.72	0.76	-	-
BS	0.9	0.84	0.94	-	-	-
YM	0.88	0.85	-	-	-	-
Ca	0.95	-	-	-	-	-

The only significant control group relationship then, is the Fe-Ca relationship. This is evidence of the utility of the Distance Correlation, as there was no such significance assigned to this bivariate relationship from the Pearson Correlation test. Therefore there is an implication of a nonlinear relationship between these parameters in the experimental group, the Pearson Correlation result for this bivariate relationship is relatively high but still not within the threshold of significance.

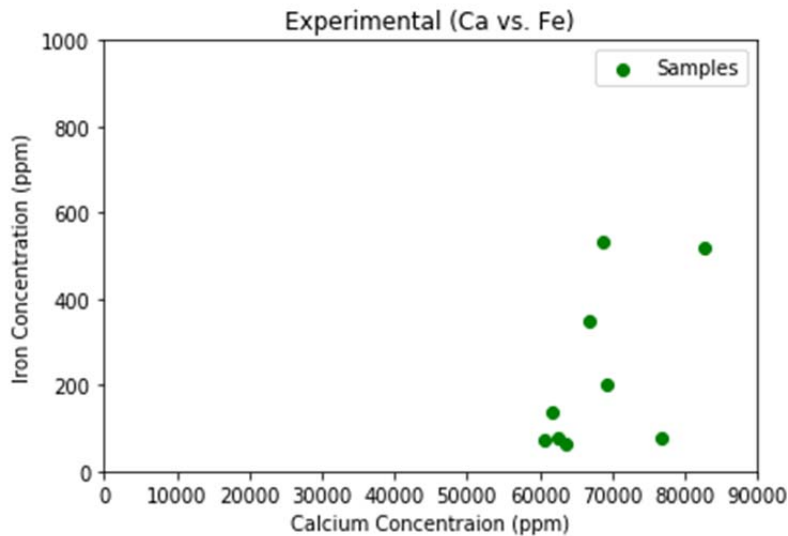


Figure 39: Scatter plot of Calcium Concentration data and Iron Concentration data from the experimental group. The 'shape' of the data can be observed.

Table 9: Székely distances between control and experimental.

\hat{d}_R	Fe	Ca	YM	BS	CD	BMD
Th	0.02	0.17	0.11	0.06	0.02	0.08
BMD	0.03	0.22	0.19	0.08	0.02	-
CD	0.04	0.12	0.13	0.09	-	-
BS	0.14	0.01	0	-	-	-
YM	0.17	0.04	-	-	-	-
Ca	0.11	-	-	-	-	-

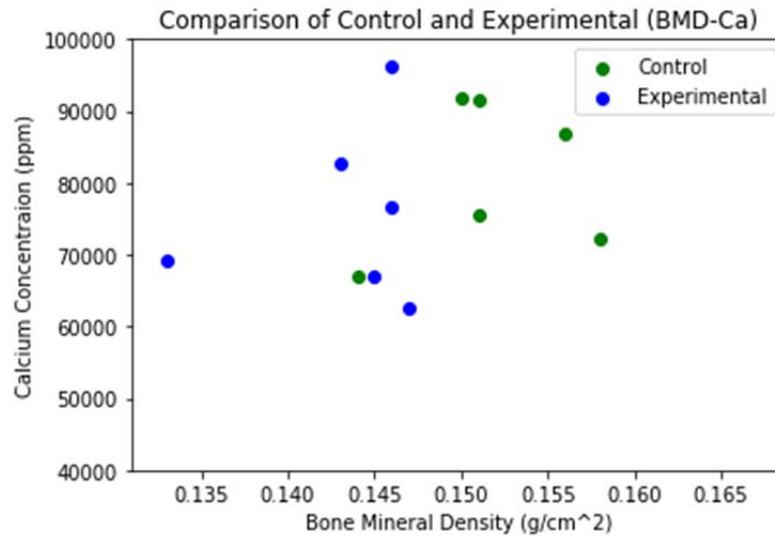


Figure 40: Scatter plot showing the control BMD-Ca results in green, and experimental results for the same parameters in blue. There is a more evident shape in the green (control) data, as most of the blue (experimental) data lie very nearly constant along the x-axis (BMD) while spreading wide along the y-axis (Ca).

An interesting point; since BMD relies on the transmission/attenuation of X-Rays through the sample and does not account for thickness in any way, one might anticipate that differences in thickness might have a great impact on the BMD result [39, 40]. However, simulations using the xpecgen package in python, with our real acquired data from the thinnest and thickest bone samples with an assumed identical bone mineral content show no change in the transmitted spectra, see figure 41 [44, 45].

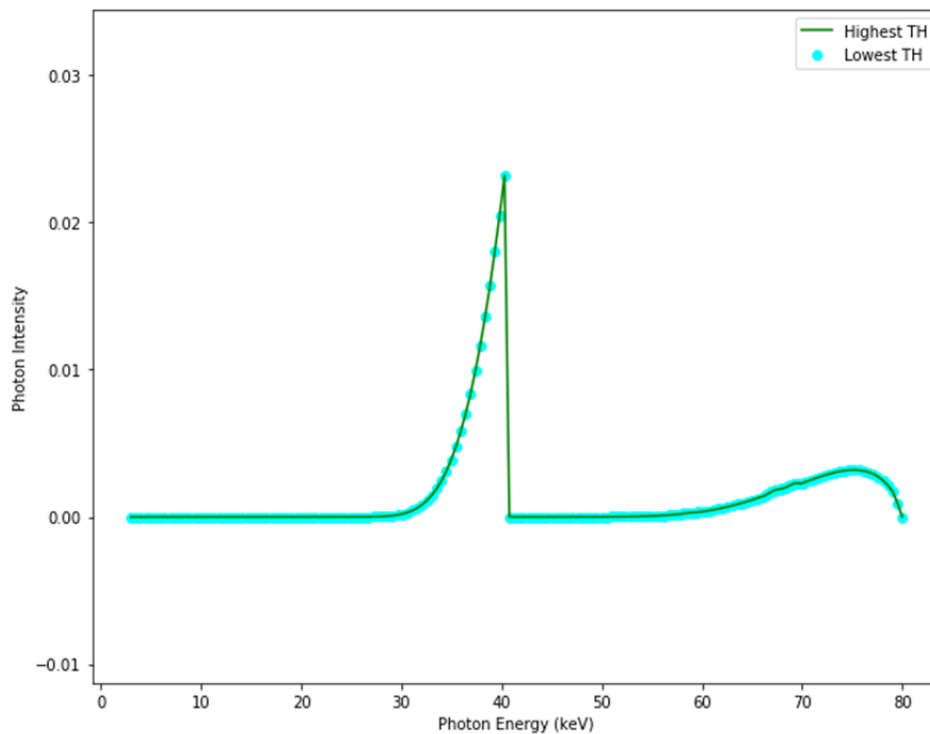


Figure 41: Plot of energy transmission spectra after passing through the highest TH (0.73mm), and lowest TH (0.43mm).

As mentioned earlier, there ought to exist some relationship between the Pearson Correlation and the Distance Correlation, given the existence of a strong linear correlation measured via the Pearson Correlation. Table 10 shows results of the difference between R and the square root of the absolute value of R for all

bivariations of parameters that meet or exceed the threshold of significance for the Pearson Correlation (R). This comes from the proposed relationship in equation 24. We can see here that when there is a strong linear correlation, the Distance Correlation tends towards the square root of the absolute value of the Pearson Correlation, with a mean value of -0.01.

Table 10: Table showing the results of differences from the proposed relationship of equation 24 for all bivariations found to be significant with the Pearson Correlation test. Notice that all values are near 0 (mean = -0.01).

$(Ca-TH)_c$	$(BS-TH)_c$	$(BMD-TH)_c$	$(CD-BMD)_c$	$(YM-BS)_c$	$(BMD-TH)_E$	$(BS-BMD)_E$	$(CD-BMD)_E$	$(Fe-YM)_E$
-0.05	0.00	-0.02	0.01	-0.08	0.01	-0.01	0.02	0.01

Equation 24: Relationship between \mathfrak{R} and R if the correlation between parameters is linear.

$$\mathfrak{R} \approx \sqrt{\|R\|}$$

Chapter 5: Conclusions

As discussed in section 3, it is proposed that calcium metabolism and storage are hampered by iron overload. One possible pathway to explain this hampering is an increased blood-level of non-transferrin bound iron (NTBI), which is common during iron overload [16,25]. NTBI refers to the presence of iron ions in biological systems, which are free to interact with ever-present phosphates (I.e. not bound to transferrin, therefore free). Specifically, the Fe-3+ ion has a high propensity of binding with phosphates to form iron-phosphate [52]. The NTBI effectively has the potential to “soak up” all available phosphate in the system, wherever NTBI is present. Phosphate is the main building block of Calcium Hydroxyapatite (CH), the compound responsible for the mineral matrix of bone. Any phosphate-dependent activity, including bone development would be subject to decreased efficiency in iron overload. As there would be less available phosphate for the production of CH, lower Ca in the experimental bones is an anticipated result. Blood NTBI levels were not measured for these works; therefore this is an accessible area for further investigation.

The Distance Correlation was shown to be a valuable tool in quantifying nonlinear relationships, and in corroborating the strong linear correlations found in the Pearson Correlation test.

The weight of the presented evidence is wholly indicative of reduced bone health in pigeons that consumed slag grit across the board. With decreases in mechanical performance, changes in the chemical and radiological makeup, the observed

structural changes, and affected parametric correlations, are all evidence that this environmental pollutant has the potential to cause harm to wild avian species.

References

- [1] G.H. Parker, G. Van Der Kraak, Use of metal-rich slag as a source of grit and its effects on pigeon health and fitness, *J. Env. Sci. Pollut. Res.* 4(2) (2018) pp 256-267.
- [2] NSL, The leaching of slag from blast furnace, National Slag Limited, Canada, 1985.
- [3] W.K. Kim, L.M. Donalson, P. Herrera, C.L. Woodward, L.F. Kubena, et al., Effects of different bone preparation methods (fresh, dry, and fat-free dry) on bone parameters and the correlations between bone breaking strength and the other bone parameters, *Poult. Sci.* 83 (2004) 1663-1666.
- [4] A. Pietrobelli, C. Formica, Z. Wang, S.B. Heymsfield, Dual-energy X-ray absorptiometry body composition model: review of physical concepts, *Am. J. Physiol. Endocrinol. Metabol.* 271(6) (1996) 941-951.
- [5] Zinke-Allmang, R. Nejat, E. Galiano-Riveros, J. Bayer, M.X. Chen, Elasticity and vibrations, In: *Physics for the Life Sciences*. 3rd E^{dn.}, Nelson Education Ltd., Canada, 2017, pp.346-351.
- [6] M. Philip, A. Nahum, J.C. Rosenwald, *Handbook of Radiotherapy Physics: Theory and Practice*, CRC Press, Boca Raton, FL, USA, 2007, pp.36-39.
- [7] E.M. Tobolski, A. Fee, Macroindentation hardness testing, In: *ASM Handbook*, Vol. 8, Mechanical testing and evaluation, ASM International, Ohio, 2000, pp.203-211.
- [8] ASTM E10-14, Standard test method for Brinell hardness testing of materials, ASTM International West Conshohocken, PA, 2014.

- [9] J. Tsay, Z. Yang, F.P. Ross, S. Cunningham-Rundles, H. Lin, et al., Bone loss due to iron overload in a murine model: importance of oxidative stress, *Blood* 116 (2010) 2582-2589.
- [10] M.C. De Vernejoul, A. Pointillart, C.C. Golenzer, C. Morieux, J. Bielakoff, et al., Effects of iron overload on bone remodeling in pigs, *Am. J. Pathology* 116(3) (1984) 377-382.
- [11] S.C. Cork, M.R. Alley, P.H.G. Stockdale, A quantitative assessment of hemosiderosis in wild and captive birds using image analysis, *Avian. Pathol.* 24 (1995) 239-254.
- [12] S.C. Cork, Iron storage disease in birds, *Avian. Pathol.* 29 (2000) 7-12.
- [13] T.K. Cheng, C.N. Coon, Effect of calcium source, particle size, limestone solubility in vitro, and calcium intake level on layer bone status and performance, *Poult. Sci.* 69(12) (1990) 2214-2219.
- [14] J.I. Orban, Factors influencing bone mineral content, density, breaking strength, and ash as response criteria for assessing bone quality in chickens, *Poult. Sci.* 72(3) (1993) 437-446.
- [15] R.J. Ward, T.C. Iancu, G.M. Henderson, J.R. Kirkwood, T.J. Peters, Hepatic iron overload in birds: analytical and morphological studies, *Avian Pathol.* 17 (1988) 451-464.
- [16] Conrad, E. Marcel, Jay N. Umbreit, Iron absorption and transport - an-update. *Am. J. Hematol.* 64(4) (2000) 287-298.
- [17] P.Y. Hester, M.A. Schreiweis, J.I. Orban, H. Mazzuco, M.N. Kopka, et al., Assessing bone mineral density in vivo: dual energy X-ray absorptiometry, *Poult. Sci.*

- 83(2) (2004) 215-221.
- [18] X.G. Cheng, G. Lowet, S. Boonen, P.H. Nicholson, P. Brys, et al., Assessment of the strength of proximal femur in vitro: relationship to femoral bone mineral density and femoral geometry, *Bone* 20(3) (1997) 213-218.
- [19] B.J. Kim, S.H. Lee, J.M. Koh, G.S. Kim, The association between higher serum ferritin level and lower bone mineral density is prominent in women \geq 45 years of age, *Osteo. Int.* 24(10) (2013) 2627-2637.
- [20] G.M. Dorrestein, G.M. Grinwis, L. Dominguez, E. Van de Jagt, A.C. Beynen, An induced iron-storage disease syndrome in doves and pigeons: a model for haemochromatosis in mynah birds? In: *Proceedings of the Association of Avian Veterinarians*, New Orleans, LA, 1992, pp.108-112.
- [21] G. Huyghebaert, Effect of dietary fluoride on performances and bone characteristics of broilers and the influence of drying and defatting on bone-breaking strength, *Poult. Sci.* 67(6) (1988) 950-955.
- [22] B. Zhang, C.N. Coon, The relationship of various tibia bone measurements in hens, *Poult. Sci.* 76(12) (1997) 1698-1701.
- [23] M.L. Samuels, J.A. Witmer, A. Schaffner, *The t-test in Statistics for the Life Sciences*, 5th E^{dn.}, Pearson Inc., USA, 2016.
- [24] P. Bevington, D.K. Robinson, *Confidence intervals in data reduction and error analysis for the physical sciences*, 3rd E^{dn.}, McGraw-Hill, USA, 2002, pp.208-210.
- [25] Brissot, Pierre, M. Ropert, C. Le Lan, O. Loréal, Non-transferrin bound iron: a key role in iron overload and iron toxicity, *Biochim. Biophys. Acta (BBA)-Gen.*

- Sub. 1820(3) (2012) 403-410.
- [26] K. Pearson, Notes on regression and inheritance in the case of two parents. Proc. Roy. Soc. London, 58 (1895) 240-242.
- [27] J. Cohen, Statistical power analysis for the behavioral sciences 2nd Ed. Laurence Earlbaum Associates, USA, (1988) 101-103.
- [28] M.H. Fulekar, Bioinformatics: Applications in Life and Environmental Sciences, Springer, Holland, 2009 110-111.
- [29] E. Galiano and M. Lapointe, Mechanical, chemical, structural, and radiological changes in pigeon bone, associated with the dietary intake of nickel recovery slag, J. Env. Sci. Pollut. Res. 5(2) (2019) 348-351.
- [30] J.H. Conway and G. Cameron, Knots and Links in Spatial Graphs. J. Graph Th. 7 (4) (1983) 445-453.
- [31] R.F. Tichy, and S. Wagner, Extremal problems for topological indices in combinatorial chemistry, J. Comp. Bio 12 (7) (2005) 1004-1013.
- [32] G. Szekely, M. Rizzo, and N. Bakirov, Measuring and testing independence by correlation of distances, Ann Stat 35(6) (2007) 2769-2794.
- [33] G. Szekely, and M. Rizzo, Brownian distance covariance, Ann Appl Stat 3(4) (2009) 1236-1265.
- [34] D. Nott, M. Tran, R. Kohn, Simultaneous variable selection and component selection for regression density estimation with mixtures of heteroscedastic experts Electron J Stat 6 (2012) 1170-1199.
- [35] R. Li, W. Zhong, L. Zhu, Feature screening via distance correlation, J Am Stat Assoc 107(499) (2012) 1129-1139.

- [36] J. Kong, B.E.K. Klein, K.E. Lee, G. Wahba, Using distance correlation and SS-ANOVA to assess associations of familial relationships, lifestyle factors, diseases, and mortality, *PNAS* 109(50) (2012) 20352-20357.
- [37] R. Klein, B.E.K. Klein, K.L. Linton, D.L. De Mets, The Beaver Dam eye study: Visual acuity, *Ophthalmology* 98(8) (1991) 1310–1315.
- [38] V. Matkovic, P.K. Goel, N.E. Badenhop-Stevens, J.D. Landoll, B. Li, J.Z. Ilich, M. Skugor, L.A. Nagode, S.L. Mobley, E.J. Ha, T.N. Hangartner, A. Clairmont, A., Calcium supplementation and bone mineral density in females from childhood to young adulthood: a randomized controlled trial. *American Journal of Clinical Nutrition* 81(1) (2005) 175–88.
- [39] M.J. Tingart, M. Apreleva, D. von Stechow, D. Zurakowski, J.J. Warner, The cortical thickness of the proximal humeral diaphysis predicts bone mineral density of the proximal humerus. *J. Bone Joint Surg.* 85 (2003) 611-617.
- [40] A.Z. LaCroix, T.J. Beck, J.A. Cauley, C.E. Lewis, T. Bassford, R. Jackson, G. Wu, and Z. Chen, Hip Structural Geometry and Incidence of Hip Fracture in Postmenopausal Women: What does it add to conventional bone mineral density? *Osteoporos Int.* 21(6) (2010) 919–929.
- [41] M.J. Silva and L.J. Gibson, Modeling the mechanical behavior of vertebral trabecular bone: effects of age-related changes in microstructure. *Bone* 21 (1997) 191-199.
- [42] J. Frimeth, E. Galiano, and D. Webster, Some Physical and Clinical Factors Influencing the Measurement of Precision Error, Least Significant Change,

- and Bone Mineral Density in Dual-Energy X-Ray Absorptiometry, *Journal of Clinical Densitometry* 13 (1) (2010) 29-35.
- [43] N.D. Priest, and F. Van de Vyver, *Trace Metals and Fluoride in Bones and Teeth*. 1st Ed. CRC Press, 1990, 234.
- [44] Hubbell, J.H. and Seltzer, S.M. (2004), *Tables of X-Ray Mass Attenuation Coefficients and Mass Energy-Absorption Coefficients*(version 1.4). [Online] Available: <http://physics.nist.gov/xaamdi> [year, month day]. National Institute of Standards and Technology, Gaithersburg, MD.
- [45] Hernández, G., Fernández F. 2016. "xpecgen: A program to calculate x-ray spectra generated in tungsten anodes." *Th* Journal of Open Source Software, 00062. doi:10.21105/joss.00062.
- [46] J. D. Hunter, "Matplotlib: A 2D Graphics Environment", *C*mputing in Science & Engineering, vol. 9, no. 3, pp. 90-95, 2007.
- [47] Kohgo, Yutaka, et al. "Body iron metabolism and pathophysiology of iron overload. *International journal of hematology* 88.1 (2008): 7-15.
- [48] *Healthcare, G. E. "Lunar enCORE-based x-ray bone densitometer user manual." (2"18).*
- [49] Pehl, R.H. Germanium gamma-ray detectors. *Phys. Today* 30, 50-61 (1977)
- [50] M. Lapointe, and E. Galiano, The Use of Different Statistical Metrics to Detect Physiological Changes in Metal-Overloaded Avian Bone, *J. Env. Sci. Pollut. Res.* 6(1) (2020) 412-416.
- [51] Taylor, J. R., and C. D. Zafiratos. *Modern Physics for Scientists and Engineers*, 1991, pp. 140, 154.

- [52] Hilton, Robert J., et al. "Phosphate inhibits in vitro Fe³⁺ loading into transferrin by forming a soluble Fe (III)–phosphate complex: A potential non-transferrin bound iron species." *Journal of inorganic biochemistry* 110 (2012): 1-7.
- [53] Goldstein, Joseph I., et al. *Scanning electron microscopy and X-ray microanalysis*. Springer, 2017.
- [54] Greenfield, S. "Inductively coupled plasmas in atomic fluorescence spectrometry. A review." *Journal of Analytical Atomic Spectrometry* 9.5 (1994): 565-592.
- [55] Vanhaecke, Frank, Martín Resano, and Luc Moens. "Electrothermal vaporisation ICP-mass spectrometry (ETV-ICP-MS) for the determination and speciation of trace elements in solid samples–A review of real-life applications from the author's lab." *Analytical and bioanalytical chemistry* 374.2 (2002): 188-195.
- [56] Novaes, Cleber Galvão, et al. "A review of multivariate designs applied to the optimization of methods based on inductively coupled plasma optical emission spectrometry (ICP OES)." *Microchemical journal* 128 (2016): 331-346.
- [57] Attix, Frank Herbert. *Introduction to radiological physics and radiation dosimetry*. John Wiley & Sons, 2008.

Appendix I

Python script, cannibalized from [45] to be used to fetch NIST database information for mass attenuation coefficients of composite materials which are not included in the xpecgen package:

```

1. from __future__ import print_function
2.
3. import requests
4. import re
5. import sys
6. from copy import deepcopy
7. import warnings
8. import numpy as np
9.
10. def _split_borders(data, border_separation=1E-8):
11.     # Positions where a border starts
12.     new_data = deepcopy(data)
13.     repeated = [index for index, values in enumerate(zip(data[:-
14.     1], data[1:])) if values[0][0] == values[1][0]]
15.     # TODO: Check excess epsilon
16.     borders_distance = [new_data[i][0] - new_data[i -
17.     1][0] for i in repeated] + [
18.     new_data[i + 2][0] - new_data[i + 1][0] for i in repeated]
19.     if borders_distance:
20.         min_distance = min(borders_distance)
21.         if min_distance < border_separation:
22.             print("The value of the border-
23.             separation parameter is too big. It has automatically been reduced.",
24.                 file=sys.stderr)
25.             border_separation = min_distance / 2
26.     for i in repeated:
27.         new_data[i][0] -= border_separation
28.         new_data[i + 1][0] += border_separation
29.     return new_data
30.
31.
32. class ElementData:
33.
34.     def __init__(self, row):
35.         self.z = int(row[0])
36.         self.symbol = str(row[1])
37.         self.name = str(row[2])
38.         self.mass_ratio = float(row[3])
39.         self.excitation = float(row[4])
40.         self.density = float(row[5])
41.
42.     def __repr__(self):

```

```

43.         return "ElementData<" + str(self.z) + ">"
44.
45.     def get_coefficients(self, use_density=False):
46.         if use_density:
47.             if self.z in [85, 87]:
48.                 print("Warning: using a density value arbitrarily set to 10
g/cm^3.", file=sys.stderr)
49.                 return fetch_coefficients(self.z, self.density)
50.             else:
51.                 return fetch_coefficients(self.z)
52.
53.
54. class CompoundData:
55.
56.
57.     def __init__(self, row, short_name):
58.
59.         self.short_name = short_name
60.         self.name = str(row[0])
61.         self.mass_ratio = float(row[1])
62.         self.excitation = float(row[2])
63.         self.density = float(row[3])
64.         # TODO: add composition information from row[4]
65.
66.     def __repr__(self):
67.         return "CompoundData<" + str(self.short_name) + ">"
68.
69.     def get_coefficients(self, use_density=True):
70.         if use_density:
71.             return fetch_coefficients(self.short_name, self.density)
72.         else:
73.             return fetch_coefficients(self.short_name)
74.
75.
76. def fetch_coefficients(z, density=None, border_separation=1E-8):
77.
78.     if density is None:
79.         density = 1
80.
81.     if type(z) is int or (type(z) is str and z.isdigit()): # Either an int
eger or a string with a natural number
82.         str_z = str(z) if int(z) > 9 else "0" + str(z) # Two digit string
83.         url = "http://physics.nist.gov/PhysRefData/XrayMassCoef/ElemTab/z"
+ str_z + ".html"
84.     else:
85.         url = "http://physics.nist.gov/PhysRefData/XrayMassCoef/ComTab/" +
z + ".html"
86.
87.     r = requests.get(url)
88.     html = r.text
89.     errored = False
90.     try:
91.         html = str(html).split("</DIV>")[2] # Pick the div with the ascii
table
92.
93.     except IndexError:

```

```

94.         errored = True
95.     if errored:
96.         raise RuntimeError("Could not recognize page structure. Check if pa
page is working:\n%s" % url)
97.     # How numbers are represented in the NIST web.
98.     number_pattern = r'-?[0-9]+\.[0-9]*E[-+][0-9]+'
99.     lines = re.findall(number_pattern + " " + number_pattern + " " + numb
er_pattern, html)
100.         data = []
101.         for l in lines:
102.             l2 = list(map(float, l.split(" ")))
103.
104.             data.append([l2[0], l2[1] * density, l2[2] * density])
105.         return _split_borders(data, border_separation) if border_separat
ion else data
106.
107.
108.     def fetch_elements():
109.
110.         url = "http://physics.nist.gov/PhysRefData/XrayMassCoef/tab1.htm
1"
111.         r = requests.get(url)
112.         html = r.text
113.         rows = re.findall(r"<TR.*?>(.*?)</TR>", html, re.DOTALL)[3:] #
Pick the rows, excluding the headers
114.         output = []
115.         for row in rows:
116.             parsed_row = re.findall(r"<TD.*?>(.*?)</TD>", row)
117.             # Remove some cells with only " " (which are only in H, prob
ably a bad formatting practice)
118.             parsed_row = list(filter(lambda s: s != " ", parsed_row))
119.             # Remove trailing spaces
120.             parsed_row = list(map(lambda x: x.strip(), parsed_row))
121.             # Dictionary entries by atomic number (as string), symbol an
d name.
122.             output.append(ElementData(parsed_row))
123.         if not output:
124.             warnings.warn("Empty list returned. Is the NIST page working
?:\n%s" % url)
125.         return output
126.
127.
128.     def fetch_compounds():
129.
130.         # First relate short names with names from the links in table 4
131.
132.         r = requests.get("http://physics.nist.gov/PhysRefData/XrayMassCo
ef/tab4.html")
133.         html = r.text
134.         cells = re.findall(r"<TD.*?>(.*?)</TD>", html, re.DOTALL)[4:] #
Pick the cells, excluding the headers
135.         cells = list(filter(lambda s: s != " ", map(lambda x: x.strip(),
cells)))
136.         # Now cells are of the form:
137.         # <A href="ComTab/adipose.html">Adipose Tissue</A> (ICRU-44)
138.         # The part after </A> being optional
139.         name_dict = {}

```

```

139.         for c in cells:
140.             data = re.findall(r'<A.*?/(.*?).html">(.*?)</A>(.*?)', c)[0]
141.             # data is a tuple with for example ('adipose', 'Adipose Tiss
ue', ' (ICRU-44)')
142.             # The last element might be the empty string.
143.             # We associate short names to names
144.             name_dict[data[1] + data[2]] = data[0]
145.
146.             # Now fetch the compound data
147.             r = requests.get("http://physics.nist.gov/PhysRefData/XrayMassCo
ef/tab2.html")
148.             html = r.text
149.             rows = re.findall(r"<TR.*?>(.*?)</TR>", html, re.DOTALL)[3:] #
Pick the rows, excluding the headers
150.             output = []
151.             errored = False
152.             for row in rows:
153.                 parsed_row = re.findall(r"<TD.*?>(.*?)</TD>", row)
154.                 # Remove trailing spaces
155.                 parsed_row = list(map(lambda x: x.strip(), parsed_row))
156.                 # Remove some cells with only " " (which are only in the fir
st element, probably a bad formatting practice)
157.                 parsed_row = list(filter(lambda s: s != " ", parsed_row))
158.                 # Dictionary entries by atomic number (as string), symbol an
d name.
159.                 try:
160.                     short_name = name_dict[parsed_row[0]]
161.                     output.append(CompoundData(parsed_row, short_name))
162.                 except KeyError:
163.                     # TODO: Manually fix these errors.
164.                     if not errored:
165.                         print("Warning: errors found the following compounds
:", file=sys.stderr)
166.                         errored = True
167.                         print("- " + parsed_row[0], file=sys.stderr)
168.                     if errored:
169.                         print("These materials are not available in the list", file=
sys.stderr)
170.                     if not output:
171.                         warnings.warn(
172.                             "Empty list returned. Is the NIST page working?:\n%s" %
"http://physics.nist.gov/PhysRefData/XrayMassCoef/")
173.                     return output
174.
175.             z = 'bone'
176.             short_name = 'bone'
177.
178.
179.             d = fetch_coefficients('tissue', density=1.060, border_separation=1E
-8)
180.             for row in d:
181.                 del row[2]
182.                 myarray = np.asarray(d)
183.                 dd = np.transpose(myarray)
184.                 ddd = dd.tolist()
185.                 print(ddd[1])

```

```
186.     np.savetxt("tissue[0].csv", ddd[0])
187.     np.savetxt("tissue[1].csv", ddd[1])
```

Appendix II

Example of script used to generate transmission spectra from a tungsten anode X-Ray tube:

```
1. from __future__ import print_function
2. import numpy as np
3. from xpecgen import xpecgen as xg
4. import matplotlib.pyplot as plt
5. from matplotlib.ticker import NullFormatter
6.
7. #Define some parameters
8. E0=80
9. theta=12
10.
11. s=xg.calculate_spectrum(E0,theta,3,160,epsrel=0.5)
12.
13. #The spectrum with cerium and tissue and bone
14. s2=s.clone()
15. s2.attenuate(0.12,xg.get_mu(13)) #1.2 mm of Al
16. s2.attenuate(100,xg.get_mu("air")) #100 cm of Air
17. s2.attenuate(0.12,xg.get_mu(58)) #1.2mm of Ce
18. s2.attenuate(4,xg.get_mu("tissue")) #some tissue
19. s2.attenuate(0.006,xg.get_mu("bone")) #some bone
20. #the spectrum with cerium
21. s3=s.clone()
22. s3.attenuate(0.12,xg.get_mu(13)) #1.2 mm of Al
23. s3.attenuate(100,xg.get_mu("air")) #100 cm of Air
24. s3.attenuate(0.12,xg.get_mu(58)) #1.2mm of Ce
25. #the spectrum with no filter
26. s4=s.clone()
27. s4.attenuate(0.12,xg.get_mu(13)) #1.2 mm of Al
28. s4.attenuate(100,xg.get_mu("air")) #100 cm of Air
29.
30. #Export the spectrum as an Excel document
31. #s2.export_xlsx(str(E0)+"keV.xlsx")
32.
33. #Interact with the spectrum using matplotlib
34. x,y = s2.get_points()
35. z,t = s3.get_points()
36. u,v = s4.get_points()
37. fig = plt.gcf()
38. #To adjust plot size
39. fig.set_size_inches(8, 6)
40. plt.xlabel("Photon Energy (keV)")
41. plt.ylabel(r"Photon Intensity")
42. plt.plot(x,y, label= "Tissue, Bone and Cerium Filtered", color= "blue")
43. plt.plot(z,t, label= "Cerium Filtered", color= "cyan")
44. plt.plot(u,v, label= "No Filter", color= "green")
45. plt.legend()
```

```
46. plt.show()
```

Appendix III

Python code used for distance correlation calculation:

```

1. #Below is an arbitrary dataset.
2.
3. x = [223, 333, 632, 1100, 5, 8821, 411, 6732, 92]
4. y = [55, 60, 61, 62, 65, 66, 82, 101, 173]
5. if len(y) != len(x):
6.     sys.exit('n must be equal in both groups!')
7. print('n =', len(x))
8.
9.
10. #Below is the calculation of the differences:
11. S = 0 #sum of whole x_j - x_k
12. N = 0 #number of differences
13. g = 0
14. while g <= (len(x)-1):
15.     h = 0
16.     while h <= (len(x)-1):
17.         S = S + abs(x[g] - x[h])
18.         h=h+1
19.         N=N+1
20.     g=g+1
21. print('x Diff Sum =', S,', Number of x Diff =', N,', Mean x Diff =', S/N)
22.
23. SS = 0 #sum of whole y_j - y_k
24. NN = 0 #number of differences
25. gg = 0
26. while gg <= (len(y)-1):
27.     hh = 0
28.     while hh <= (len(y)-1):
29.         SS = SS + abs(y[gg] - y[hh])
30.         hh=hh+1
31.         NN=NN+1
32.     gg=gg+1
33. print('y Diff Sum =', SS,', Number of y Diff =', NN,', Mean y Diff =', SS/N
N)
34.
35.
36. #Below dVar = dVar_x is found:
37. def calcMDist(x, n):
38.     MDist = 0
39.     for i in range(len(x)):
40.         MDist += abs(x[i]-x[n])
41.     return MDist
42. Amatsq = [[0.0 for i in range(len(x))] for j in range (len(x))]
43. for i in range(len(x)):
44.     ci = calcMDist(x, i)/len(x)
45.     for j in range(len(x)):
46.         cj = calcMDist(x, j)/len(x)

```

```

47.     a = abs(x[j] - x[i])
48.     Amatsq[i][j]= (a - ci - cj + S/N)**2
49. sAsq=0
50. for i in range(len(x)):
51.     for j in range(len(x)):
52.         sAsq += Amatsq[i][j]
53. dVar = (sAsq/len(x)**2)**0.5
54.
55.
56. #ddVar = dVar_y:
57. def calcMMDist(y, m):
58.     MMDist = 0
59.     for ii in range(len(y)):
60.         MMDist += abs(y[ii]-y[m])
61.     return MMDist
62. AAmatsq = [[0.0 for ii in range(len(y))] for jj in range (len(y))]
63. for ii in range(len(y)):
64.     cii = calcMMDist(y, ii)/len(y)
65.     for jj in range(len(y)):
66.         cjj = calcMMDist(y, jj)/len(y)
67.         aa = abs(y[jj] - y[ii])
68.         AAmatsq[ii][jj]= (aa - cii - cjj + SS/NN)**2
69. sAAsq=0
70. for ii in range(len(y)):
71.     for jj in range(len(y)):
72.         sAAsq += AAmatsq[ii][jj]
73. ddVar = (sAAsq/len(y)**2)**0.5
74.
75.
76. #Finding dCov and dCor
77. sAB=0
78. for i in range(len(x)):
79.     ii = i
80.     for j in range (len(x)):
81.         jj = j
82.         sAB += ((Amatsq[i][j])**0.5)*((AAmatsq[ii][jj])**0.5)
83. dCov = (sAB / (len(x)*len(y)))**0.5
84. dCor = dCov/((dVar*ddVar)**0.5)
85. print('dCor =',dCor)

```